PCCP

PAPER

View Article Online
View Journal | View Issue

Cite this: *Phys. Chem. Chem. Phys.*, 2026, **28**, 5894

Validity of kinetic predictions for polymer crystallization from molten and glassy states: the case of poly(*p*-dioxanone)

Roman Svoboda

The crystallization of poly(*p*-dioxanone) (PDX) was examined under different regimes – cooling of a melt, heating from the glassy state, and isothermal annealing reached either from the melt or from the glass. In addition to differential scanning calorimetry (DSC) measurements, supplemental characterization was performed using Raman spectroscopy, thermogravimetry, and optical microscopy. The comparison of the hot and cold crystallization data revealed distinct differences in the PDX crystallization behavior, governed by the presence/amount of nuclei generated on the applied thermal path. The kinetic analysis of the crystallization data employed the extended autocatalytic model combined with Hoffman–Lauritzen or Arrhenius rate expressions. Both frameworks fitted the data well, but their predictive accuracy depended strongly on how the temperature-dependent nucleation $K_g(T)$ and growth $E(T)$ activation energies were implemented (an improvement of the existing models was suggested, based on compensation *via* the addition of a continuous temperature dependence of the pre-exponential factor $A(T)$). Predictions of isothermal crystallization from non-isothermal kinetics were only reliable when the nucleation state of the system was appropriately reproduced, underscoring the limitations of using thermal proximity alone as a predictor.

Received 7th December 2025,
Accepted 2nd February 2026

DOI: 10.1039/d5cp04749h

rsc.li/pccp

1. Introduction

The process of crystallization in polymers plays a pivotal role in practically all applications of semi-crystalline thermoplastics, *i.e.*, polymers with regular, linear chain structure, small, symmetrical side groups, and strong intermolecular interactions (*e.g.*, hydrogen bonding). In practice, the crystallization of these polymers occurs either from the glassy state upon heating or from the molten state upon cooling. These two distinct pathways are central to how polymers are processed and used in manufacturing, packaging, medical devices, and structural components.

Crystallization from the molten state during cooling is fundamental to the primary shaping processes of polymers, such as injection molding, extrusion, and blow molding. For example, in the production of polyethylene terephthalate (PET) bottles, the rate and extent of crystallization during cooling directly affect the bottle's mechanical strength, clarity, and barrier properties. If PET crystallizes too quickly, it may become opaque and brittle; if it crystallizes too slowly or insufficiently, the product may be too soft or deform under load. Control over melt crystallization is therefore essential for ensuring dimensional stability and performance.[1,2] Several other examples involve the following: polypropylene (PP) injection molding, where the cooling rate affects spherulite size, transparency, and toughness: fast cooling leads to smaller spherulites (improved toughness), while slow cooling enhances stiffness but reduces impact strength;[3] high-density polyethylene (HDPE) pipe manufacturing, where melt crystallization determines pipe rigidity, long-term creep resistance, and thermal performance: improper cooling can lead to uneven crystallinity and dimensional instability;[4] polyamide 6 (Nylon 6) in automotive parts, where the crystallinity developed during cooling enhances strength, heat resistance, and chemical durability;[5] polyethylene naphthalate (PEN) for high-performance films, which requires controlled crystallization to achieve superior dimensional stability and gas barrier properties in packaging and electronics;[6] thermoplastic polyurethane (TPU) moldings, where the crystallized hard segments influence mechanical properties and shape memory behavior in applications like medical catheters and wearable electronics;[7] polyketone (PK) fibers require control of the crystalline morphology, critical for high-performance products used in filtration and reinforcement;[8] polyoxymethylene (POM/Acetal) crystallization determines low friction and wear-resistant surfaces in precision gear applications;[9] melt-spun polyethylene terephthalate (PET) fibers are crystallization-

---

Department of Physical Chemistry, Faculty of Chemical Technology, University of Pardubice, Studentská 573, 532 10 Pardubice, Czech Republic. E-mail: roman.svoboda@upce.cz

affected with respect to tenacity and shrinkage—crucial for textiles and industrial fibers;[10] crystalline polylactic acid (PLA) packaging (specifically compostable hot food containers) utilizes development of the semi-crystalline phase during slow cooling to improve thermal resistance;[11] quality of the polybutylene terephthalate (PBT) crystalline phase ensures dimensional precision, flame resistance, and insulation properties for electrical connectors and housings.[12]

On the other hand, crystallization from the glassy state during heating (also called ''cold crystallization'') becomes relevant for polymers that are initially processed into the amorphous state through, *e.g.*, rapid quenching or solvent casting. For example, during 3D printing, the polymers are often printed amorphous or only partially crystallized to maintain flexibility and ease of shaping, as is the case with polylactic acid (PLA) used to manufacture medical implants.[13,14] The consequent controlled crystallization realized *via* thermal annealing increases the stiffness, mechanical stability, and resistance to hydrolytic degradation, so that the implant remains functional for the period of time required for the patient to heal. The cold crystallization is paramount also in the powder-based processing, such as the technique of selective laser sintering (typically polyamides PA12, PA11, and PA6, and thermoplastic polyurethanes (TPU)), where the laser-sintered amorphous particles undergo post-processing heat treatment, enhancing the mechanical strength and dimensional accuracy of the printed part.[15–17] Furthermore, in pharmaceutical applications, the semi-crystalline polymer excipients (*e.g.*, polyethyleneglycol (PEG) or poly(ε-caprolactone) (PCL)) are tailor-crystallized to fine-tune the drug release profiles.[18,19] For medicinal polymers, such as poly(*p*-dioxanone) (PPDX) used for the manufacturing of biodegradable sutures and implants, the properties of the crystalline phase embedded in the amorphous matrix define not only the mechanical properties but also the rate of degradation.[20] In recycling, post-processing and re-processing, the thermal annealing is used to restore the crystallinity lost during the previous re-extrusion or aging; common examples include poly(ethylene terephthalate) (PET) used for various packaging needs, or poly(trimethylene terephthalate) (PTT) used for textile manufacturing.[21,22]

From the physico-chemical point of view, polymer crystallization proceeds during the cooling of the melt as a kinetically regulated, multistage ordering process, reflecting a competition between thermodynamic driving forces and molecular constraints imposed by chain connectivity. With the initiation of undercooling, local density, conformational, and orientational fluctuations emerge in the melt. At the microscopic level, nucleation is initiated by the cooperative alignment of chain segments into transient, partially ordered clusters.[23–27] In many polymers, this early ordering manifests as a mesomorphic state, characterized by enhanced segmental orientation and conformational regularity without full three-dimensional translational order, which arises due to the segmental alignment and conformational selection being kinetically accessible on shorter time scales than long-range registry and lamellar organization. The mesomorphic domains reduce the nucleation barrier by lowering interfacial free energy with the surrounding melt and often act as precursors or self-nuclei for subsequent crystallization.[24–29] The consequent crystal growth then proceeds through the incorporation of chain segments from the surrounding amorphous matrix into lamellar crystals, requiring chain folding, partial disentanglement, and transport toward the growth front.[23,24,28–32] These processes are inherently frustrated by limited chain mobility, leading to non-ideal folding, loop and tie-chain formation, and lamellae with finite thickness and defects. As crystallization progresses, the development of crystalline domains imposes spatial and dynamic constraints on the remaining amorphous material, giving rise to a rigid amorphous fraction (RAF) in which chains are immobilized by interfacial confinement rather than structural order. Simultaneously, volumetric contraction and differential mobility generate a mechanically strained amorphous matrix, with residual stresses and frozen-in orientation reflecting the non-equilibrium nature of the transformation.[26–32]

On the other hand, the crystallization of the amorphous polymer (formed *via* melt-quench) proceeds during heating from the already present frozen-in structural heterogeneities that were formed during the preceding cooling phase. The potentially formed mesomorphic domains may persist below the glass transition (T_g) as kinetically trapped, partially ordered regions – upon reheating above T_g, the domains regain mobility and can act as very efficient self-nuclei, promoting rapid nucleation without the need for large-scale molecular rearrangements.[27,30–32] Crystal growth then proceeds from these pre-aligned segments, often leading to high nucleation densities and comparatively imperfect lamellar structures. Contrary to the crystallization proceeding during cooling, the structural/spatial frustration associated with the RAF formation gets immediately released with rising temperature within the cold-crystallization regime.[27,30–32]

The final semicrystalline morphology therefore encodes the entire kinetic pathway of cooling (and consequent heating) – the nucleation (either homo- or heterogeneous) can be further mesophase-mediated, which can enhance the crystal density, the associated imperfect growth yields folded and defective lamellae, and the coexistence of mobile amorphous, rigid amorphous, and crystalline regions produces a heterogeneous material whose mechanical and thermal properties are governed as much by frustrated molecular packing as by crystalline order itself.[24,30,31]

As shown above, the two distinct crystallization pathways play a crucial role in polymer technology and science. Owing to the intricacies associated with the multi-degree ordering of the polymer matrix (as opposed to, *e.g.*, inorganic or low-molecular organic glasses), the prediction of the crystallite morphology, density, and distribution is not straightforward with regard to these two pathways. With the detailed knowledge of the crystallization process being crucial for a large number of applications utilizing thermoplastic polymers, this topic deserves to be explored. Owing to the processing route for the majority of thermoplastics, the theoretical framework for the description of crystallization from the melt[23–28] has been developed to a significantly greater extent compared to crystal growth from the amorphous phase, where (largely) the ordinary Arrhenian dependence of the rate constant[29–32] is utilized to describe the crystallization kinetics. Note that both these approaches to kinetic analysis will be introduced in detail in Section 2. With the very recent development and thorough testing of a universal kinetic model[27,28] for polymer crystallization, the possibility of critically comparing the two approaches to crystal growth in polymers is now open. Even more importantly, the accuracy of the kinetic predictions provided by these two approaches can now be directly confronted with experimental results to determine the best way of tailoring the crystallization process in practice.

Such analysis is the main goal of the present paper. Since the experimental crystallization data need to be collected in all standardly utilized regimes (*i.e.*, non-isothermally during the cooling of a melt, non-isothermally during the heating of a glass, isothermally after cooling from a melt, isothermally after heating from a glass), the choice of suitable polymeric materials is rather limited. In the present work, the crystallization behavior of poly(*p*-dioxanone) (PDX) will be exploited in this regard. This material was shown[32] to exhibit a relatively broad temperature interval, in which the crystallization can be initiated both during cooling from the molten state and during heating from the glassy state (which is the base requirement of the present research). In addition, PDX exhibits[32] well resolved polymorphic transitions, formation of the RAF phase, and was even reported to be able to form the mesomorphic phase.[33] As such, PDX is a suitable model candidate for exploration of the variations (both kinetic and physicochemical ones) associated with crystal formation *via* the two distinct pathways. Apart from PDX being used as a model material, the crystallization data and the corresponding predictions will also be of practical interest, since PDX is used for the manufacturing of chirurgical sutures,[34,35] and is currently considered for the production of various medicinal implants.[35,36]

2. Theoretical background

The kinetics of the simple thermally activated solid-state processes (including crystal growth) can be described by the following set of equations,[29] where eqn (1a) is the universal expression used for the solid-state kinetics (multiplication of the rate constant K and kinetic model f), and eqn (1b) is one of the most common and flexible kinetic models, the Šesták–Berggren equation:[29,37]

$$\frac{\mathrm{d}\alpha}{\mathrm{d}t} = K(T)\cdot f(\alpha) \tag{1a}$$

$$f(\alpha) = (1-\alpha)^N \cdot \alpha^M \tag{1b}$$

In these equations, $\mathrm{d}\alpha\cdot\mathrm{d}t^{-1}$ is the rate of conversion from the amorphous to crystalline phase (with α being the degree of conversion scaled between 0 and 1, and t being time), $K(T)$ is the rate constant (only temperature-dependent), and M and N are the kinetic exponents responsible for the autocatalytic (M) and reaction order (N) behaviors, respectively. In particular, the exponent M is primarily associated with delayed crystal growth; the delayed onset of the crystallization process is then partially balanced by the faster (autocatalyzed) course of the process (once it is initiated) so that the peak width (temperature range in which the process occurs) is largely reduced.[27,29,37] The physicochemical interpretation of such influence on the crystallization behavior includes factors such as the presence of pre-existing nuclei or crystalline phase in general, the presence of impurities, nanoparticles, or phase-separated domains, the presence of moisture with plasticizing effect, the products of oxidative or decomposing reactions, internal or external mechanical stress, exposure to radiation, electrical or magnetic fields, or effects affecting the material's surface or volume mobility (self-diffusion) – including the structural relaxation.[30,38–43] The exponent N then only affects the endset tail of the crystallization peak, prolonging it at increasing N value. The low N values (<0.65) indicate the transition from the standard nucleation-growth crystallization mechanism to the contracting-sphere kinetics (growth from a large number of surface nuclei with the front propagating at a constant rate inwards the material grain).[29,30,38–43] On the other hand, $N > 1.2$ indicates a deceleration of the final crystallization stages due to, *e.g.*, spatial restrictions, internal stresses arising from the preceding formation of the crystalline phase, or a broad distribution of nucleation site quality; one of the major reasons for such behavior can also be the secondary crystallization.[30,38–43]

As mentioned in the introductory section, the fundamental difference between the two approaches to modeling the hot and cold crystallization lies in the expression of the rate constant $K(T)$. The crystal growth from the molten phase is usually described in terms of the Hoffman–Lauritzen theory:[23,24]

$$K(T) = A\cdot\exp\left(-\frac{U^*}{R(T-T_\infty)}\right)\exp\left(-\frac{K_\mathrm{g}}{T\Delta T f}\right) \tag{2}$$

where A is a pre-exponential factor (defining the relationship between the microscopic and macroscopic manifestation of crystal growth), U^* is the activation energy for the segmental movements of the polymer chains (6300 J mol^{-1} for the majority of polymeric materials[23]), R is the universal gas constant (8.314 J K^{-1} mol^{-1}), T_∞ is the temperature below which all motions associated with a viscous flow are supposed to be significantly longer than the given experimental time scale for the crystal growth (customarily $T_\infty = T_\mathrm{g} - 30$ °C, where T_g is the glass transition temperature), ΔT is the undercooling (defined as $\Delta T = T_\mathrm{m}^\mathrm{eq} - T$, where T_m^eq is the equilibrium melting temperature), f is the correction factor defined as $f = 2T/(T_\mathrm{m}^\mathrm{eq} + T)$, and K_g is the Hoffman–Lauritzen nucleation constant (the kinetic parameter associated with nucleation):[23]

$$K_\mathrm{g} = \frac{w_\mathrm{n} d \sigma_\mathrm{l} \sigma_\mathrm{f} T_\mathrm{m}^\mathrm{eq}}{\Delta H_\mathrm{m}^\mathrm{V} k_\mathrm{B}} \tag{3}$$

where w_n is a constant associated with the nucleation regime, d is the thickness of a lamellar monolayer, σ_l and σ_f are the lateral/lamellae and chain fold free surface energies, respectively, k_B is the Boltzmann constant, and ΔH_m^V is the volumetric equilibrium melting enthalpy. Contrary to the Hoffman–Lauritzen expression of $K(T)$, the ordinary thermally activated solid-state kinetics commonly utilizes the Arrhenius dependence:[44]

$$K(T) = A \cdot \exp\left(-\frac{E}{RT}\right) \quad (4)$$

where E is the activation energy of the crystal growth and A is the pre-exponential factor (generally similar in meaning but different in the absolute value from the similar quantity from eqn (2)). It is immediately apparent that the Arrhenius-defined $K(T)$ represents a simple exponential increase with increasing T, not accounting for the decrease of the crystallization rate below T_m due to the lack of the driving force (expressed by ΔT in eqn (2)). This issue can be partially solved by introducing temperature dependent $E(T)$ and $A(T)$ into eqn (4) – as was shown in ref. 45. It is also noteworthy that only the non-monotonous $K(T) - T$ dependence (be it the Hoffmann–Lauritzen or Arrhenius with implemented $E(T)$ and/or $A(T)$) can produce the experimentally observed effect,[27,45] when the asymmetry of the crystallization peak significantly changes with applied heating/cooling rate. This further justifies the utilization of $E(T)$ and $A(T)$ in eqn (4). The added flexibility can be, of course, matched by a similar feature in the case of the Hoffman–Lauritzen, where the crystal growth proceeding near or above the onset inflection point of the $K(T) - T$ dependence results in akin change of the asymmetry of the crystallization peak (see ref. 27 and 46). A further increase of flexibility for the Hoffman–Lauritzen approach can also be achieved by introducing a K_g–T dependence into eqn (2) – this possibility will be (among others) explored in detail in Section 5.1.

3. Experimental

Poly(*p*-dioxanone) (PDX) sutures (MediCross, Ostrava, Czech Republic) were used as a source of the PDX polymer and were used as-purchased. The main portion of experimental measurements was performed by means of differential scanning calorimetry (DSC), using the Q2000 calorimeter (TA Instruments, USA) equipped with an autosampler and RCS90 cooling accessory. The measurements were performed in the *T*-zero heat flow mode; the DSC was calibrated utilizing the melting temperatures and enthalpies of the In, Zn, and H_2O standards; the calibrations were performed under standard conditions (hermetically sealed low-mass Al pan with a pin-hole lid, purge gas (N_2) flow of 20 cm^3 min^{-1}, heating rate q^+ = 10 °C min^{-1}). The PDX pieces cut from the original suture were hermetically sealed in a low-mass *T*-zero Al pan, which is a commercial type of 40 μl Al pan with a mass of ~20.4 mg and a corresponding lid (~10.3 mg) for hermetical sealing (the experiments were thus effectively performed in a static air atmosphere). The sample masses varied in the 10.0–10.2 mg range (determined with ±0.05 mg accuracy).

Four series of cyclic DSC measurements were performed, each with a new sample to avoid the degradation (thermal depolymerization[32]) that slowly occurs above the melting temperature T_m. In particular, each of the four temperature programs consisted of a series of cycles (starting with cooling from the molten state, and finishing with heating into the molten state), where a selected variable(s) was changed for each cycle. In the following paragraphs, the four types of temperature programs (always corresponding to one cycle) will be described, with the visual representations given in Fig. 1.

(1) Cyclic non-isothermal experiments with hot crystallization occurring during the cooling of the molten PDX, where the sample was first annealed for 30 s at 130 °C, then cooled at a selected cooling rate q^- (which was the only variable in this type of cycle; the cooling rate followed the order 50, 30, 20, 15, 10, 7, 5, 3, 2, 1, 0.5, 0.2, and 0.1 °C min^{-1}) to −35 °C, and then heated back to 130 °C at 20 °C min^{-1}. Note that these cycles were also performed as a test of the critical cooling rate for PDX.

(2) Cyclic non-isothermal experiments with cold crystallization occurring during the heating of the glassy PDX, where the sample was first annealed for 30 s at 130 °C, then cooled at 50 °C min^{-1} to −35 °C, and then heated at a selected heating rate q^+ (varying in the order 50, 30, 20, 15, 10, 7, 5, 3, 2, 1, 0.5, 0.2, and 0.1 °C min^{-1}) to 130 °C.

(3) Cyclic isothermal experiments being initiated by cooling from the molten state, where the sample was first annealed for 30 s at 130 °C, then cooled at 50 °C min^{-1} to a selected annealing temperature T_a with an isotherm following for the time t_a; then the sample was cooled to −30 °C at 10 °C min^{-1}, and then heated to 130 °C at 10 °C min^{-1}. The following T_a in °C (t_a in min) combinations were used for the performed cycles: 50(60), 45(60), 40(60), 35(60), 30(60), 25(60), 20(60), 15(60), 10(60), 5(120), 0(240).

(4) Cyclic isothermal experiments being initiated by heating from the glassy state, where the sample was first annealed for 30 s at 130 °C, then cooled at 50 °C min^{-1} to −30 °C, then heated at 50 °C min^{-1} to a selected annealing temperature T_a with an isotherm following for the time t_a; then the sample was cooled to −30 °C at 10 °C min^{-1}, and then heated to 130 °C at 10 °C min^{-1}. Identical T_a (t_a) combinations as for the cycle of the third type were used.

Thermal stability of PDX was (apart from the complex evaluation of the DSC data) directly assessed by thermogravimetry (TGA), using the STA (TGA) 449 F5 Jupiter instrument (Netzsch) equipped with a DSC/TG holder. In this regard, two simple heating scans were performed under air and N_2 atmospheres (flow rate 50 cm^3 min^{-1}) in the 30–550 °C temperature range (at a heating rate of 10 °C min^{-1}). The TGA measurements were realized in open Al pans (40 μl, ~21.5–22 mg); the sample masses were ~10 mg (determined with ±0.005 mg accuracy). The structural characterization of selected PDX samples was done by means of Raman spectroscopy, using the DXR2 Raman microscope (Thermo Fisher Scientific, USA) equipped with a 785 nm excitation diode laser (laser spot size 1.6 μm) and a CCD detector. The measurements were

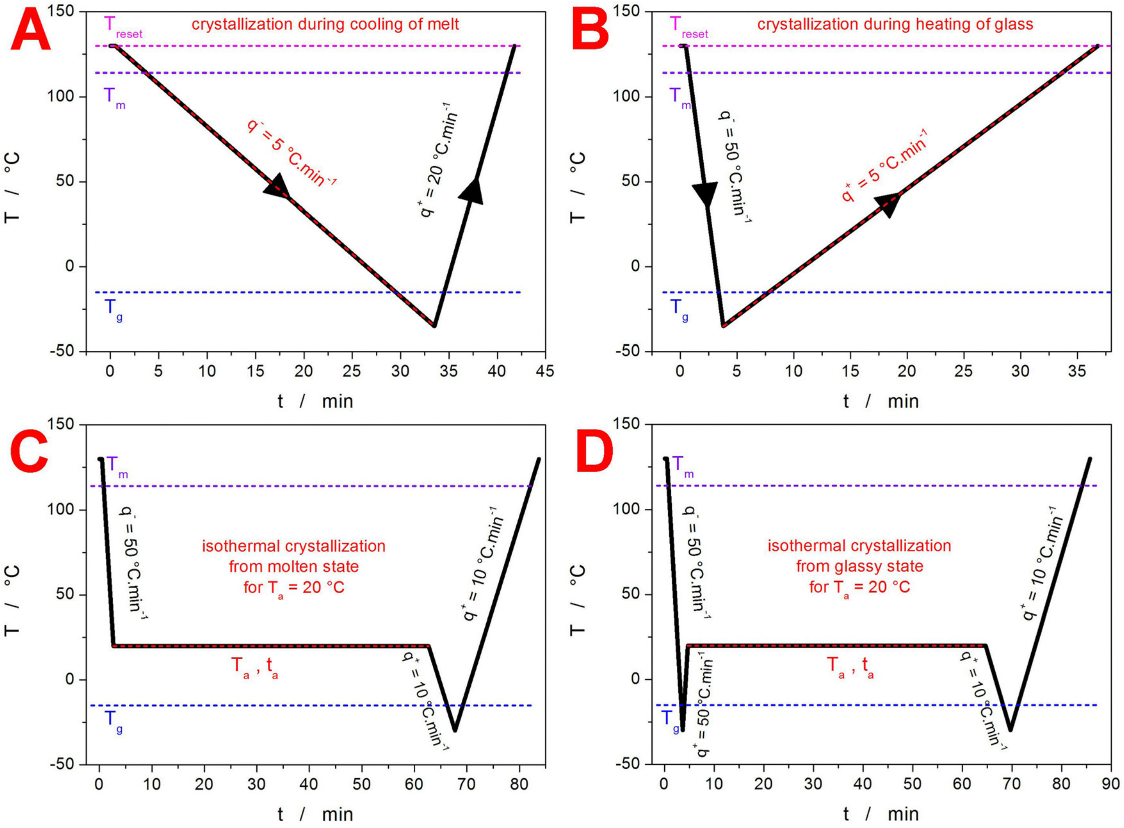

Fig. 1 (A)–(D) Visual representation of the four types of temperature programs (always a single cycle) applied to study the crystallization behavior of PDX. The quantities in red indicate the variables within each type of experiment.

performed with 20 mW laser power on the sample, 3 s duration of a single scan, and 35 scans accumulated in one spectrum, in the spectral range of 50–3375 cm^{-1}. In addition, the selected PDX samples were also investigated with respect to crystalline morphology by means of optical microscopy, using the iScope PLMi (Euromex) optical microscope in the transmission mode, equipped with a series of ×4–×40 objectives and a Moticam visual camera (with a ×1 magnification adapter).

4. Results

The main part of the experimental results was obtained by DSC – the non-isothermal crystallization data obtained during cooling and heating are depicted in Fig. 2A and B, respectively; several examples (every other measurement) of the isothermal crystallization curves are shown in Fig. 2C and D. Starting with the experiments focused on crystallization during the cooling of the melt (Fig. 2A, variable q^-, fixed q^+ = 20 °C min^{-1}), it is clear that at the highest cooling rate of 50 °C min^{-1}, practically no crystallization proceeds, as almost no detectable signal occurs during the cooling part of the cycle and a large crystallization peak is recorded during the consequent heating scan. Interestingly, the heating scan following the cooling at q^- = 50 °C min^{-1} does not exhibit the highest crystallization enthalpy; a slightly stronger crystallization peak occurs during heating following the cooling at q^- = 30 °C min^{-1}, which provides an ideal balance between nucleation (the lower the q^-, the more time provided for nucleation) and crystal growth (the lower the q^-, the more time provided for crystal growth, which then does not already contribute to the exothermic signal evolving during the consequent heating). The borderline cooling rate is q^- = 10 °C min^{-1}, which is the lowest q^- during which full crystallinity is not achieved during cooling. Note that by "full crystallinity" we are referring to the standard value of $\chi_c \approx$ 45–55% achievable for this semi-crystalline polymer;[47] the corresponding melting enthalpy of a fully crystalline PDX was determined to be $\Delta H_{m100\%}$ = 141.18 J g^{-1}.[48] The heating curves following the individual cooling steps then exhibit an endothermic glass transition effect characterized by the glass transition temperature T_g of ∼−10 °C, followed by the exothermic crystallization signal (manifesting at ∼25–55 °C for the preceding $q^- \geq$ 10 °C min^{-1}) and the endothermic melting signal (manifesting between ∼95 and 120 °C). Depending on the prior q^-, a small secondary crystallization peak closely preceding the melting process can occur. This crystallization peak is attributed to the polymorphic $\alpha' \rightarrow \alpha$ or disorder → order transition (where α' represents a mesomorphic phase with loose chain packing, which forms at low T). Correspondingly, the $\alpha' \rightarrow \alpha$ transition is missing during the cycles with low q^-, where the majority of the crystalline phase was formed at high T (just below the melting temperature T_m).

The second set of non-isothermal DSC measurements is depicted in Fig. 2B – with variable q^+ and fixed $q^- = 50\ ^\circ\mathrm{C\ min^{-1}}$. Since all cooling steps were performed at maximum q^-, a practically fully amorphous PDX was always formed, and the consequent heating scans were typologically identical, with the effects only shifting to higher T with increasing q^+. The only small exception was the cycle performed at the highest q^+, where the secondary high-T crystallization ($\alpha' \rightarrow \alpha$ transformation) is missing. This is either because the primary crystallization already proceeded at high enough T (due to q^+ being $50\ ^\circ\mathrm{C\ min^{-1}}$) for only a negligible amount of the α' phase being formed, or because at such high q^+, the melting of the α' phase was initiated before it could recrystallize into the α polymorph. A very interesting discrepancy (crucial for the topic of the present paper) was found when monitoring the isothermal crystallization at high T_as – see Fig. 2C. Whereas in the case of cold crystallization (during the heating of the glassy phase), the process gradually slowed down as T_a decreased, the hot crystallization (proceeding during the cooling of a melt) exhibited a non-monotonous trend in the crystallization rate, where the process was slower for $T_\mathrm{a} = 50\ ^\circ\mathrm{C}$, sped up for T_as = 40 and 30 °C, and then again significantly slowed down at even lower T_as, roughly evening out the rates of both processes at $T_\mathrm{a}\mathrm{s} \leq 20\ ^\circ\mathrm{C}$. The seemingly anomalous behavior observed for the hot crystallization is caused by the absence of pre-existing nuclei when crystallizing on the path from the molten state. In the case of cold crystallization, the prior formation of the PDX glass (during the cooling at $q^- = 50\ ^\circ\mathrm{C\ min^{-1}}$) produces a fixed amount of nuclei, and the consequent crystal growth then proceeds from this approximately constant number of active sites. On the other hand, during hot crystallization, the nucleation and crystal growth processes proceed simultaneously, where the former is the rate-limiting step at high T. This explains not only the much higher crystallization rates during the high-T cold crystallization, but also the $G_{T=30^\circ\mathrm{C}} > G_{T=50^\circ\mathrm{C}}$ data (with "G" being the macroscopic crystallization rate), indicating that the contributions of the nucleation and crystal growth rates even out in the 30–40 °C temperature range. This will be further referred to in Section 5.1 during the mathematical modeling of the two phenomena. As mentioned above, at low T ($\leq 20\ ^\circ\mathrm{C}$), the DSC-recorded crystallization rates are roughly similar for both crystallization paths (cold and hot), meaning that a sufficiently high number of nuclei was formed during the cooling to these temperatures regardless of the selected path, reaching a saturated state.

In this regard, an even more interesting finding is that associated with the isothermal crystallization at 0 °C, where the sample crystallizing directly after cooling from the melt

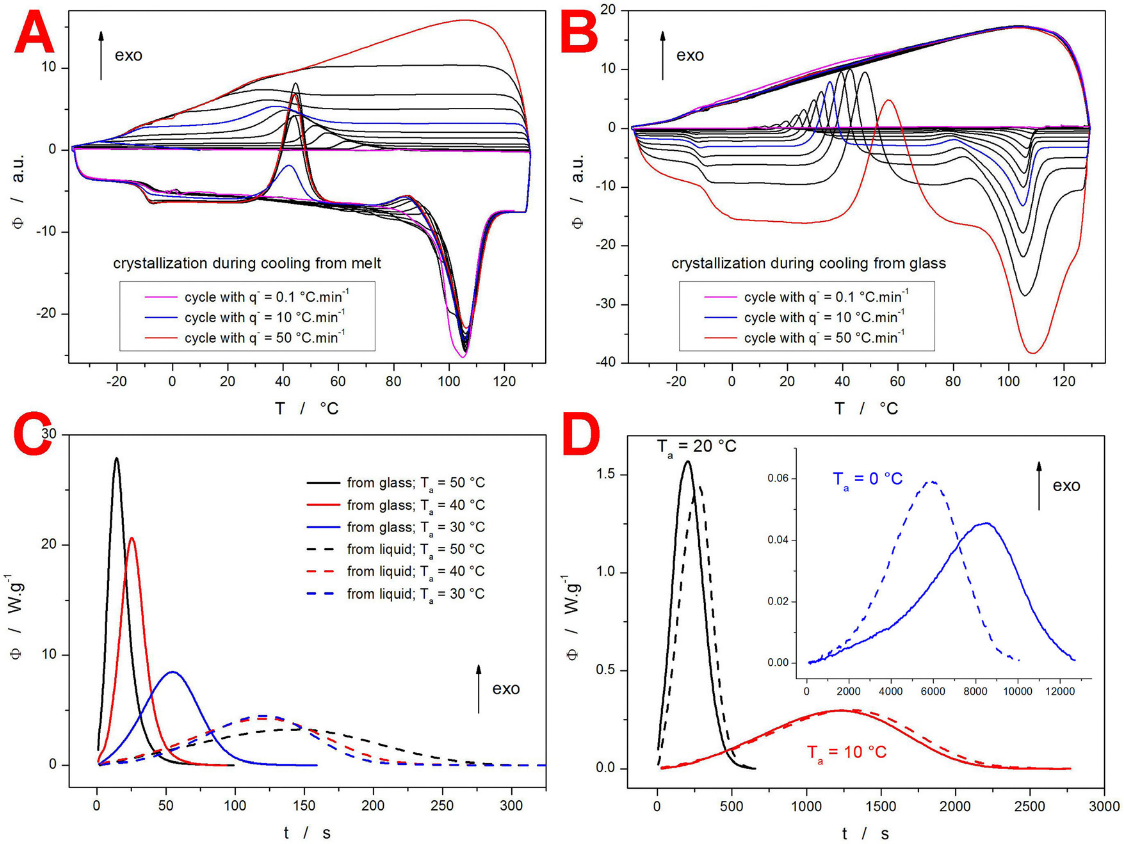

Fig. 2 (A) and (B) Raw non-isothermal DSC data – cycles for selected q^-/q^+ are indicated. (C) and (D) Selected isothermal crystallization data from within high and low T_as (every second T_a is depicted). The meaning of the solid and dashed lines is similar in both graphs. In all graphs, exothermic effects evolve in the upward direction.

crystallized faster, but to a significantly lower extent. Whereas the latter can be partially explained by possible inaccuracies in the baseline subtraction, the faster crystallization rate clearly means that the microscopic crystal growth rate is already very low at these temperatures, and that it is the nucleation rate which dictates the crystallization behavior. In particular, the very high density of nuclei formed in the case of the glass-quenched sample hinders the overall crystallization process, as the impingement occurs very early and the competition over the available polymer chains slows down the reordering process. In addition, the nucleation-dominated crystallization could also explain the final difference in the reached crystallinity degrees, as a larger portion of the amorphous matrix can be eventually converted into the crystalline lamellae.

Since certain important parts of Fig. 2A and B are not clear due to the scaling/overlap of the raw data cycles, the selected archetypal heating scans are shown in greater detail in Fig. 3A and B (not necessarily corresponding to the parts of Fig. 2A and B). In Fig. 3A, the trend in the shape of the melting peak measured during the heating scan following the cooling at different q^- (shown in Fig. 2A) is depicted for the low q^- cycles. Evidently, the high-T crystallization manifesting at low q^- results in an absence of the $\alpha' \rightarrow \alpha$ transformation (as the majority of the crystalline phase is already formed at high T, and thus as an α polymorph).

In addition, the high-T crystallization also results in the manifestation of the lower-T melting peak shoulder, which gets further split depending on the actual applied q^-. We believe that these multiple shoulders correspond to the gradual formation of the rigid amorphous fraction (RAF; as opposed to the mobile amorphous fraction (MAF)[49–51]) that characterizes the interface between the crystal and the true amorphous phase – note that this layer is formed by the semi-fixated parts of polymer chains, which are already not included in the folded crystalline lamellae. The main/dominant melting peak shoulder then indicates the formation of an additional distinct crystalline phase (high-temperature polymorph/stable phase) – deeper insight into this behavior is reported in ref. 32 and 52. As can be seen in Fig. 3A, the first signs of the $\alpha' \rightarrow \alpha$ transformation are apparent for the cycle with $q^- = 2$ °C min^{-1}, where the hot crystallization proceeded in the 45–80 °C temperature range, as opposed to the $q^- = 1$ °C min^{-1} cycle with 55–85 °C range. The high-temperature limit for the formation of the α' phase thus appears to be ∼55–60 °C. The differences in the low-q^- and high-q^- cycles are further contrasted in Fig. 3B, with the added comparison to the typical heating scan following the isothermal crystallization measurement at $T_a = 40$ °C. The typical feature associated with the heating scans following the isothermal crystallization is the presence of a small endotherm (often characterized as a hybrid process between the glass transition and melting) slightly above T_a corresponding to the stabilization of the RAF phase.[52,53] It is worth noting that none of the DSC experiments provided direct evidence for the formation of the mesomorphic phase in PDX (apart from the above-mentioned $\alpha' \rightarrow \alpha$ or disorder → order transition), which should manifest as a broad and weak

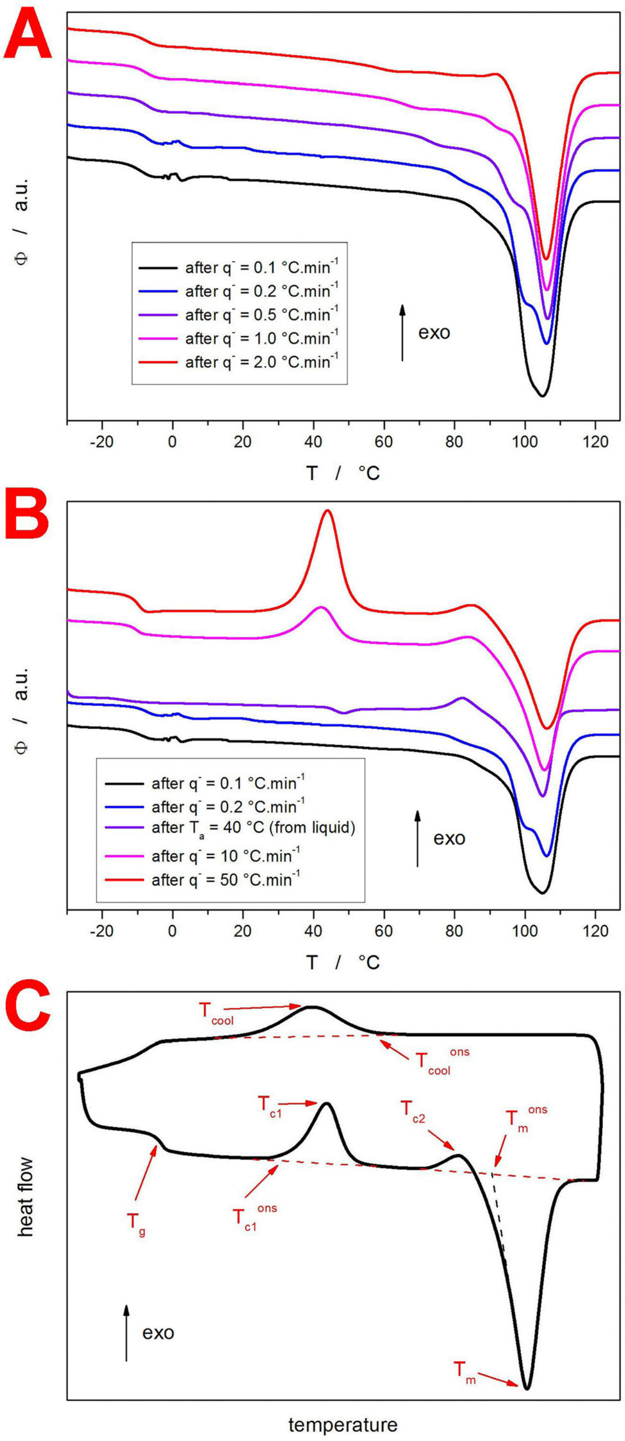

Fig. 3 (A) Zoom-in on the DSC heating curves following the cooling steps at low q^- (measured during the cycles with crystallization occurring during the cooling of the melt). (B) Archetypal heating scans selected out of all measured data (defining the responses observed within all four types of cyclic experiments). (C) Definition of terminology associated with characteristic temperatures and enthalpies evaluated for the DSC measurements. The red dashed lines indicate the integration of the peak areas; the black dashed line indicates the evaluation of the extrapolated onset of the main melting peak. In all graphs, the exothermic effects evolve in the upward direction.

exothermic signal. Nonetheless, the nonexistence of such signal does not prove the nonexistence of the mesomorphic phase, the formation of which can be simply associated with too slow heat evolution (below the DSC detection limit) or be hidden as an underlying signal overlapping with stronger-manifesting physico-chemical phenomena.

To quantify the different types of thermokinetic behavior depicted in Fig. 2, evolution of the trends in characteristic temperatures and enthalpies was determined – the terminology associated with the evaluated processes is schematically defined in Fig. 3C, where the dashed lines indicate the evaluation of the crystallization and melting enthalpies. Note that T_g was evaluated as a half-height midpoint, and the upper index "ons" corresponds to the quantity being evaluated as an extrapolated onset temperature. The trends in characteristic quantities linked with the non-isothermal measurements (Fig. 2A and B) are shown in Fig. 4, and the evaluation of the isothermal data is presented in Fig. 5. The data in tabular form are included in the SI.

Starting with the cold crystallization data (Fig. 2B), the corresponding trends depicted in Fig. 4A show that the most pronounced changes are those in $T_\mathrm{c1}^\mathrm{ons}$, T_c1, T_c2, ΔH_c1, and ΔH_m. Whereas the characteristic temperatures behave with increasing q^+ as is commonly expected (rapid increase of T_c1 due to the low activation energy, slow increase of T_g due to the high activation energy, practically invariable T_m that only slightly changes as a consequence of the ratios of different polymorphic phases), the opposite trends in the crystallization and melting enthalpies are more interesting. The increasing ΔH_c1 with increasing q^+ can be partially a consequence of Kirchhoff's law, but as will be shown below, the main contribution still has to be associated with the low-T mesomorphic α' with loose chain packing exhibiting a generally lower ΔH_c1. The seeming discrepancy with ΔH_m then arises from the overlap between secondary crystallization and melting. If one neglects the possible inaccuracies associated with the loss of the *exo*/*endo* signals due to their overlap, then the low q^+ generally produces a larger amount of the α' phase, and this larger portion then recrystallizes at high temperature to form the more densely packed α polymorph, which consequently translates into the higher overall melting enthalpy – note that the measured melting peak reflects the final state after the secondary (c2) recrystallization, rather than the original primary (c1) crystallization process.

The evaluation of the hot crystallization cycles (raw data depicted in Fig. 2A) is shown in Fig. 4B and C. In Fig. 4B, the evaluation of the (second) heating part of the cycles is shown (purposefully before the first, cooling step), where the T_c1 and ΔH_c1 data start only at $q^- = 7$ °C min^{-1} (at lower q^-, full crystallinity was achieved already during the first, cooling parts of the cycles). Since all the heating scans were performed at the same $q^+ = 20$ °C min^{-1}, no major variability of the characteristic temperatures can be expected. Hence, instead of plotting T_g, the difference of heat capacity between the undercooled liquid and glassy states (Δc_p; evaluated at T_g) is shown. This quantity corresponds to the degree of crystallinity achieved after the first, cooling part of the cycle was finished. Again, the sharp increase of Δc_p for cycles with $q^- > 10$ °C min^{-1} indicates that at these cooling rates, highly/fully amorphous PDX material was obtained. The corresponding evaluation of the first cooling steps is shown in Fig. 4C. If we sum the crystallization enthalpies ΔH_cool (the portion achieved during the cooling step) and ΔH_c1 (the portion achieved during the consequent heating), the resulting value nicely copies the trend for the melting enthalpy ΔH_m. In the case of the hot crystallization cycles, the majority of the crystal formation occurs (at least at low q^-) during cooling; hence, the situation is simpler compared to the previously

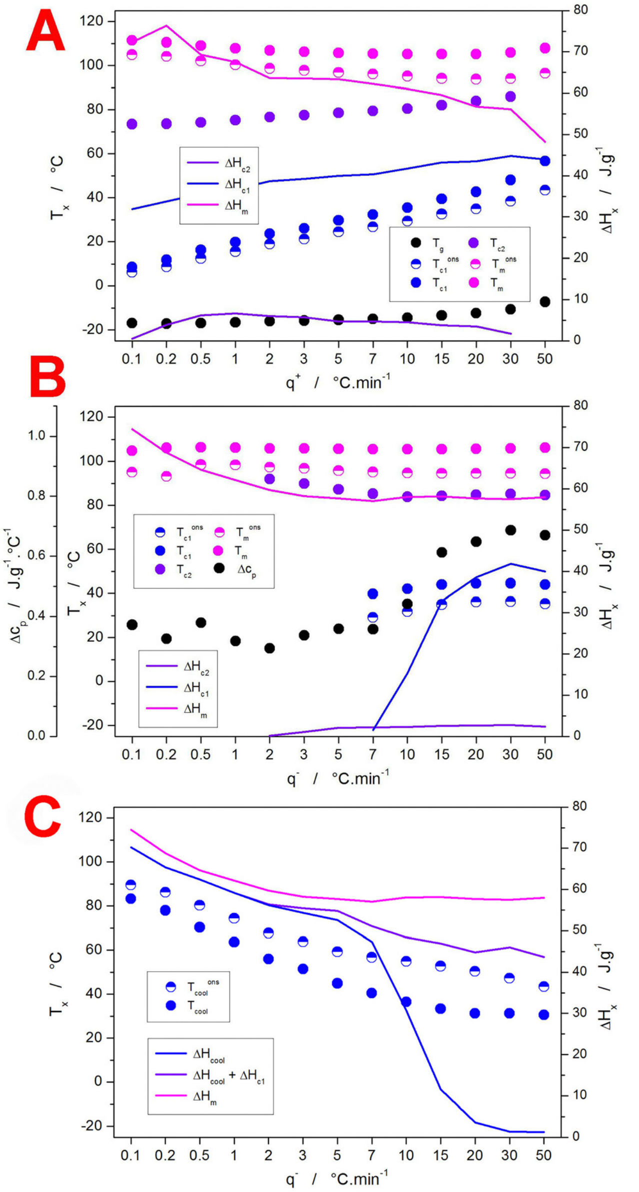

Fig. 4 (A) Characteristic temperatures and enthalpies obtained during the melt-cooling crystallization cycles. (B) Characteristic temperatures and enthalpies obtained during the heating parts of the glass-heating crystallization cycles. (C) Characteristic temperatures and enthalpies obtained during the cooling parts of the glass-heating crystallization cycles + a comparison of the main enthalpic responses.

discussed cold crystallization cycles. During slow cooling of the melt, the crystallization occurs at high *T*, a large portion of the densely packed α polymorphic phase is formed, and the crystallization as well as the corresponding melting enthalpies are similarly high, because no α′ → α recrystallization occurs. At higher q^-, a significant portion of the crystalline phase is still formed (or at least pre-nucleated) during the cooling step, which defines the similarity between $\Delta H_{\mathrm{cool}} + \Delta H_{\mathrm{c1}}$ and ΔH_{m}. The higher the q^-, the lower the portion of the crystalline phase being formed during the cooling step, and hence, the increasing discrepancy between the two enthalpies – see the magenta and violet lines in Fig. 4C.

The characteristics monitored during the heating scans following the isothermal crystallization steps (where T_{a} was achieved either by rapid cooling of a melt or by rapid heating of a glass) are shown in Fig. 5. The heating scans were, again, performed at a constant q^+ = 10 °C min^{-1}; hence, the characteristic temperatures are practically invariable. Since the T_{a} range covered only the low-*T* region (0–50 °C), the determined ΔH_{m} also stays rather invariant, which is in good correspondence with the data shown in Fig. 4B and C. In general, the heating scans following both types of isothermal crystallization experiments (differing in the pathway to T_{a}) were extremely similar, exhibiting almost identical T_x and ΔH_x values.

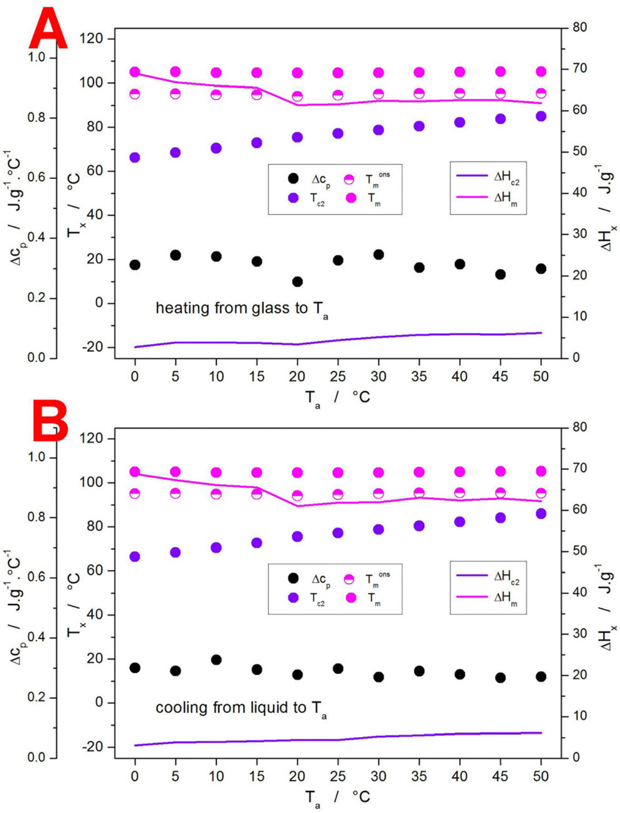

Fig. 5 (A) Characteristic temperatures and enthalpies obtained during the isothermal crystallization measurements with T_{a} achieved by heating from the glassy state. (B) Characteristic temperatures and enthalpies obtained during the isothermal crystallization measurements with T_{a} achieved by cooling from the molten state.

In addition to the DSC measurements, the selected DSC-crystallized samples were characterized by means of temperature-resolved Raman spectroscopy – see Fig. 6. The full-range Raman spectra of the molten and crystalline PDX samples are shown in Fig. 6A. The main bands can be attributed as follows: the band at 870 cm^{-1} corresponds to the C–O–C symmetric stretching vibration; the band at 1048 cm^{-1} corresponds to the stretching vibration of C–C in the aliphatic chain; the band at 1451 cm^{-1} corresponds to the –CH$_2$– bending vibration; the band at 1732 cm^{-1} corresponds to the C=O stretching vibrations in the ester carbonyl group; and the bands at 483, 1242, 1403, 1610 and 1638 cm^{-1} correspond to the vibrations in the solvent violet 13 (dye) structure.[54–56] It has been hypothesized in ref. 54 that the amount of the amorphous content in PDX can be linked to the proportional manifestation of the high-frequency shoulder of the 1732 cm^{-1} band.

In Fig. 6B, the Raman spectra are shown that were collected during the following experiment: a small PDX sample was first melted, then quenched at q^- = 50 °C min^{-1} to −30 °C (forming an amorphous matrix), and then left to "fully" crystallize at 20 °C. It is clear that, indeed, the fully amorphous PDX (be it in a liquefied or in a quenched-in form) shows a broad, round band in the 1710–1780 cm^{-1} range – to the authors' knowledge, these are the first ever recorded Raman spectra of fully amorphous PDX. As the sample crystallized, a sharp band at 1732 cm^{-1} started to form. In Fig. 6C, the Raman spectra of the fully amorphous and different DSC-crystallized samples are compared – note that in all cases the crystallized samples were "fully" crystalline (the sample cooled at q^- = 10 °C min^{-1} to −30 °C was left to crystallize to equilibrium at 20 °C; the sample heated at 50 °C min^{-1} to 70 °C was annealed at that temperature for 30 min and then cooled to laboratory temperature). It is apparent that the proportional manifestation of the two bands directly reflects the presence of the densely packed α polymorphic phase – note that the overall degree of crystallinity changes in a much less pronounced way with the conditions (temperature program) relevant for the samples depicted in Fig. 6C. Nonetheless, further confirmation of this hypothesis is necessary, as the true degree of crystallinity reached during some of these experiments can be only estimated from the present DSC data due to the involvement of the α′ → α recrystallization before the melting enthalpy associated with the low-*T* crystalline state can be determined.

As the present DSC experiments were performed in hermetically sealed Al pans, *i.e.*, in a static air atmosphere, the high-*T* PDX stability in air needed to be verified (the kinetic study of the thermal decomposition/depolymerization of PDX reported in ref. 32 was only performed under a N$_2$ atmosphere). The comparison of the TGA measurements performed in N$_2$ and air atmospheres is shown in Fig. 6D. The decomposition/depolymerization evidently proceeds slightly faster and *via* a distinctly varied mechanism in the air atmosphere, but the difference is still only by 10–20 °C, which makes the presently used upper boundary of the DSC cycles (130 °C) a safe temperature to remain at for several tens of minutes[32] – the present total of

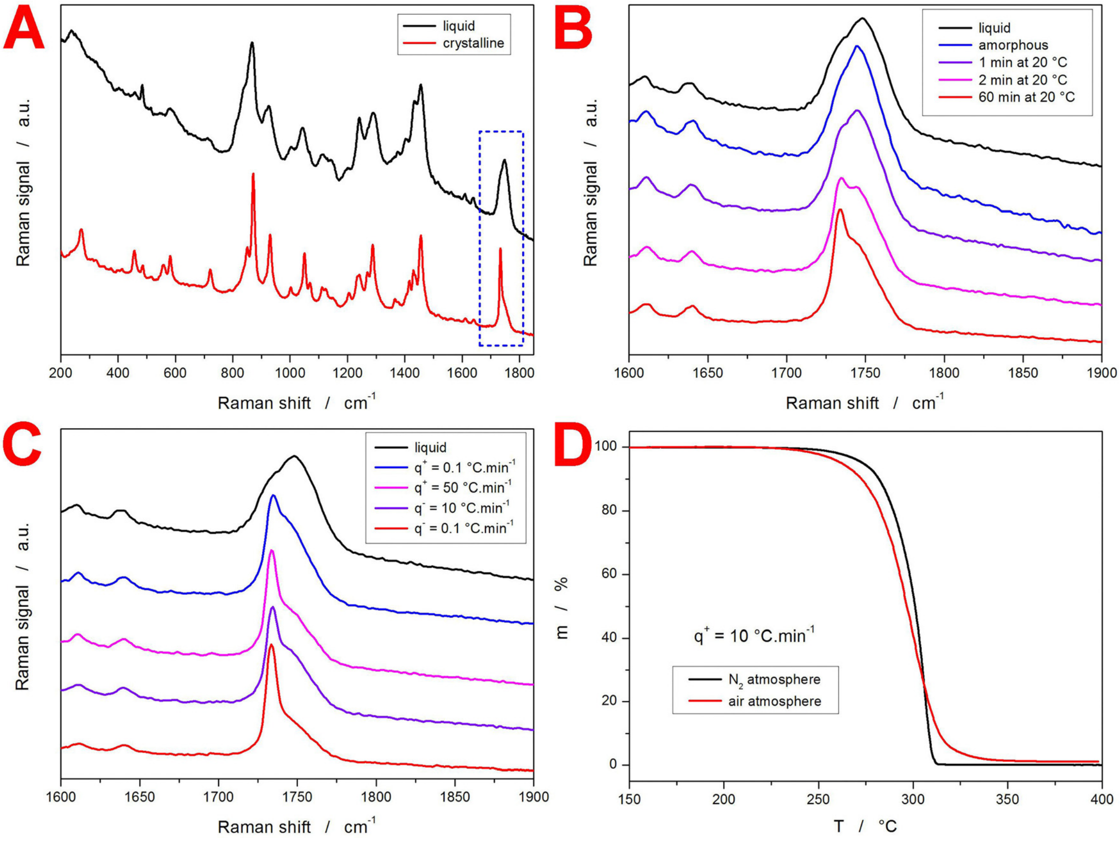

Fig. 6 (A) Raman spectra obtained for the liquefied and fully crystalline PDX samples. The characteristic band at 1732 cm^{-1} later used to consider the sample crystallinity is indicated. (B) Evolution of the 1732 cm^{-1} Raman band as the liquefied sample was quenched into the amorphous state and then left to isothermally crystallize at 20 °C. (C) Comparison of the 1732 cm^{-1} Raman bands measured for the liquefied and different non-isothermally crystallized PDX samples (q^- and q^+ indicate the crystallization occurring during melt-cooling and glass-heating, respectively). (D) TGA mass loss data for the PDX samples heated under N_2 or synthetic air atmospheres.

annealing time at 130 °C was for each sample ~8 min + the time spent in the near vicinity of the borderline temperature during the slow heating or cooling scans. It is noteworthy that no signs of sample depolymerization were detected during the DSC experiments.

Complementary data to the Raman spectroscopy measurements were obtained by means of optical microscopy. In particular, the four differently DSC-crystallized samples from Fig. 6C were photographed immediately after finishing the defined temperature program – see Fig. 7. Interestingly, the distinct spherulitic morphology with visible lamellae orientation forms only at high T during the very slow cooling of a melt ($q^- = 0.1$ °C min^{-1}). Still recognizable but significantly smaller crystallites form during the faster cooling of the melt ($q^- = 10$ °C min^{-1}). If the melt is quench-amorphized, no spherulites of comparable size (visible under ×10 magnification) can be found in the micrographs, regardless of the crystallization temperature. This is a particularly important finding with regard to the intensity of the 1732 cm^{-1} Raman band (see Fig. 6C) – the Raman-detected degree of crystallinity is not correlated to the presence of visually identifiable morphology.

5. Discussion

As was mentioned in the introductory part, the discussion will be split into two parts. First, the crystallization kinetics will be calculated for all DSC-measured crystal growth modes and pathways. The emphasis will be put on the accuracy of the model-fitting-based description of the crystallization data, as well as on the identification of the kinetic trends occurring with the key conditions of the given temperature programs (q^-, q^+, and, ultimately, T_a). In the second part, the kinetic predictions calculated on the basis of each non-isothermal path type will be compared, and their accuracy will be evaluated based on the comparison with the isothermal data.

5.1. Crystallization kinetics

5.1.1. Cooling from the melt. The DSC data (the cooling steps) shown in Fig. 2A were described in terms of the MCHL model (combination of eqn (1) and (2)). To achieve an accurate description of the DSC data, the crystallization signal needs to be separated from the thermo-kinetic background. In this regard, the tangential area-proportional baseline[29] can be

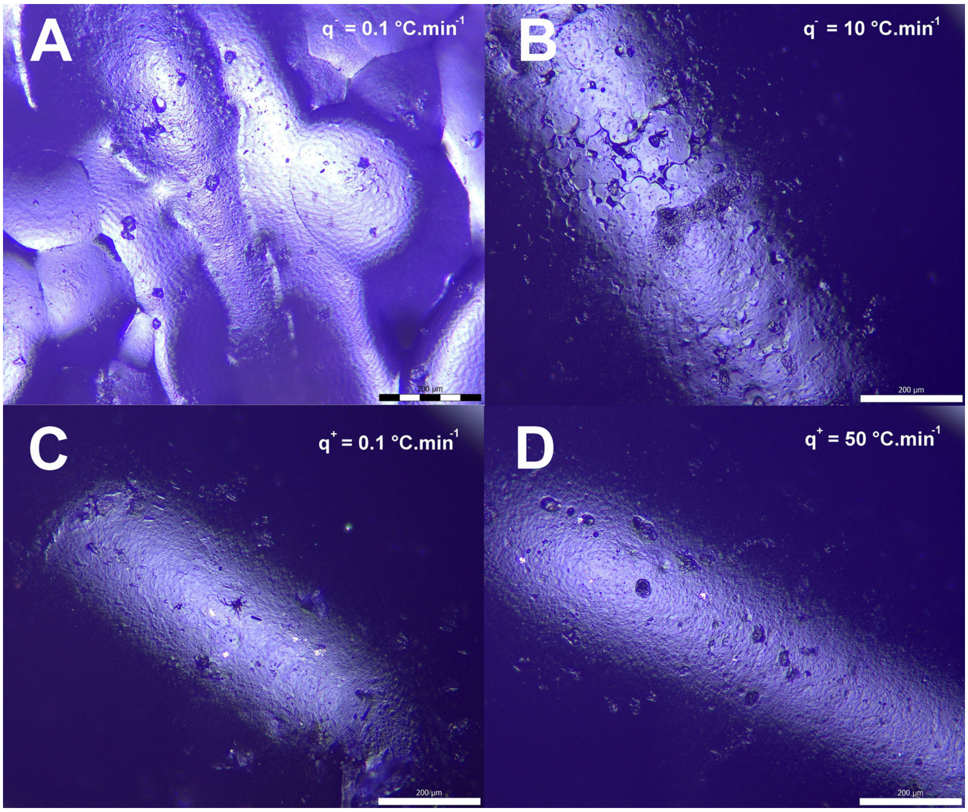

Fig. 7 (A)–(D) Optical micrographs obtained for the surface of differently crystallized PDX samples (q^- and q^+ indicate the crystallization occurring during melt-cooling and glass-heating, respectively). The scale bars indicate 200 μm length.

applied; note that this is the only commonly used baseline with a true physico-chemical background:

$$B(T) = (1 - \alpha(T))\cdot(z_{0,r} + z_{1,r}\cdot T) + \alpha(T)\cdot(z_{0,p} + z_{1,p}\cdot(T_f - T)) \quad (5)$$

where $B(T)$ is the temperature dependence of the baseline curve, α is the degree of conversion, $z_{0,r}$ and $z_{1,r}$ are the coefficients characterizing the tangent going through the starting point (in the reactant area), $z_{0,p}$ and $z_{1,p}$ are the coefficients characterizing the tangent going through the endpoint (in the product area), and T_f is the endpoint temperature. The separated exothermic crystallization peaks can be further processed to determine the nucleation constant K_g, which is essential for the physically meaningful interpretation of the nucleation/crystallization behavior. The determination of K_g is done *via* the so-called $t_{0.5}$-method based on the following equation:[23,57]

$$\ln(1/t_{0.5}) + \frac{U}{R(T_c - T_\infty)} = \ln A - \frac{K_g}{T_{0.5}\Delta T_f} \quad (6)$$

where $t_{0.5}$ and $T_{0.5}$ are the time and the temperature associated with α = 50% (meaning of the other symbols is identical to eqn (2)). For PDX, the values of T_∞ = −45 °C (derived from T_g = −15 °C) and T_m^{eq} = 114 °C (determined as the endset of the melting peak obtained at the lowest q^-) were used. The evaluation according to eqn (6) is shown in Fig. 8A; the q^-/T-dependent K_g was then determined by deriving the curved dependence associated with the left and bottom axes in this graph. Apparently, the K_g changes quite dramatically according to this evaluation, between ~80 and 1025 kK^2. However, when input into the theoretical simulation based on the combination of eqn (1) and (2), the obtained continuous K_g–T dependence results in unrealistic distortions of the rate constant, and (consequently) of the whole simulated crystallization peak. Hence, for the purpose of the non-linear optimization (based on the Levenberg–Marquardt algorithm[58,59]), K_g had to be fixed for each fit at a constant discrete value corresponding to the given crystallization data-curve (these K_g values are shown in Fig. 8A in relation to the top and right axes). In this way, each q^- had attributed its own value of K_g, resulting in a different temperature dependence of the rate constant $K(T)$ – two examples are shown in Fig. 8B together with the corresponding crystallization peaks fit by the MCHL model (with the given K_g = const. and the corresponding $K(T)$ implemented). It is noteworthy that at higher q^-, the crystallization peaks almost fully overlap with the $K(T)$–T dependence (not being positioned only at their onset edges), which results in a characteristic distortion of the crystallization data[27,45] – the asymmetry of the crystallization peaks shifts to higher α values, *i.e.*, to lower T in the case of the cooling experiments. The full set of MCH-fit DSC crystallization peaks obtained during the cooling of the melt is depicted in Fig. 8C and D.

The curve-fitting by the MCHL model (depicted in Fig. 8C and D) gave the sets of kinetic parameters that are introduced in Fig. 8E and F in dependence on q^- (and listed in SI). At low

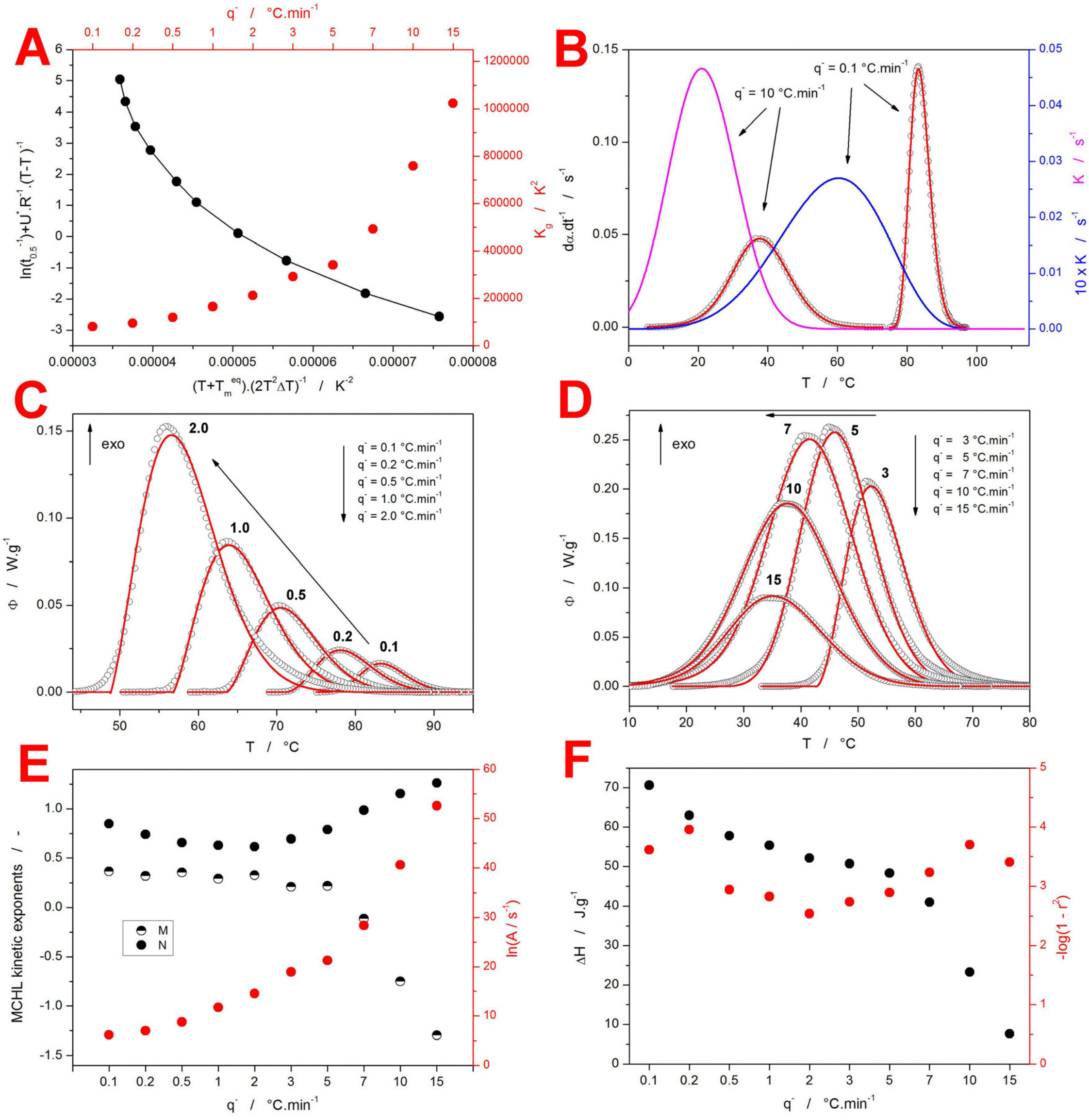

Fig. 8 (A) Determination of K_g from the melt-cooling DSC crystallization experiments (left and bottom axes); evolution of K_g with applied q^- (top and right axes). (B) Comparison of the positions of the melt-cooling crystallization peaks (points and red MCHL fitting curves) and the temperature dependence of the corresponding rate constants K (blue and magenta curves). (C) Low-q^- DSC data (points) fit by the MCHL model (red lines). (D) High-q^- DSC data (points) fit by the MCHL model (red lines). (E) and (F) Evolution of different kinetic parameters obtained from the MCHL fit of the melt-cooling crystallization data from graphs C and D.

q^-, fairly standard crystallization behavior is observed, with the MCHL parameters M and N being close[46] to the typical nucleation-growth kinetics[60,61] (in this case characterized by the Avrami exponent ~1.5). However, at $q^- \geq 7\ ^\circ\mathrm{C\ min}^{-1}$, both kinetic exponents deviate from the approximately constant values – the main feature being the exponent M attaining negative values. Note that since the exponent M is responsible for the autocatalytic behavior, its negative value indicates the mathematical autoretardation (decreasing the crystallization rate with the increasing degree of conversion α), which is the only way how (with fixed K_g value) to account for the overall decreasing crystallization enthalpy (see the identical trend for ΔH in Fig. 8F). The alternative ways of modeling this behavior would be either an implementation of the mutually compensating K_g–T and A–T dependence, or a complex reaction mechanism based on reversible reactions (with the former reflecting the true physico-chemical kinetics more closely). Nonetheless, the development of such a model/description is beyond the scope of the present paper. A partially compensating factor is also expressed by the $\ln A$ parameter; however, the negative M values are indeed paramount for allowing the description to be based on such high K_g values. The achieved accuracy of the kinetic description for all fitted data-curves is very high (the correlation coefficients are shown in Fig. 8F), confirming the relevancy of the determined kinetic parameters – note that the MCHL kinetic model has, in general, a pronounced absolute minimum in the hyperspace of the least-squares-based optimization solutions, with no comparable local minima offering acceptable alternatives. We have also tested that the very high K_g values determined for the high q^- DSC data are indeed the only possibility how to accurately describe the data with constant/fixed K_g (no other MCHL kinetic parameter can supplement the role of K_g) – this further validates the results depicted in Fig. 8A, E and F.

5.1.2. Heating from the glass. To describe the non-isothermal DSC data obtained during the heating from the glassy state, the standard approach is based on the Arrhenian rate constant, *i.e.*, the combination of eqn (1) and (4). First, the thermo-kinetic background was again subtracted from the raw DSC data using the tangential area-proportional baseline (eqn (5)). Second, the temperature-dependent activation energy $E(T)$ was determined by the Kissinger method:[62]

$$\ln\left(\frac{q^+}{T_p{}^2}\right) = -\frac{E}{RT_p} + \text{const.} \tag{7}$$

where T_p is the temperature corresponding to the maximum of the DSC crystallization peak. The Kissinger plot for the present data (raw variant depicted in Fig. 2B) is shown in Fig. 9A – the

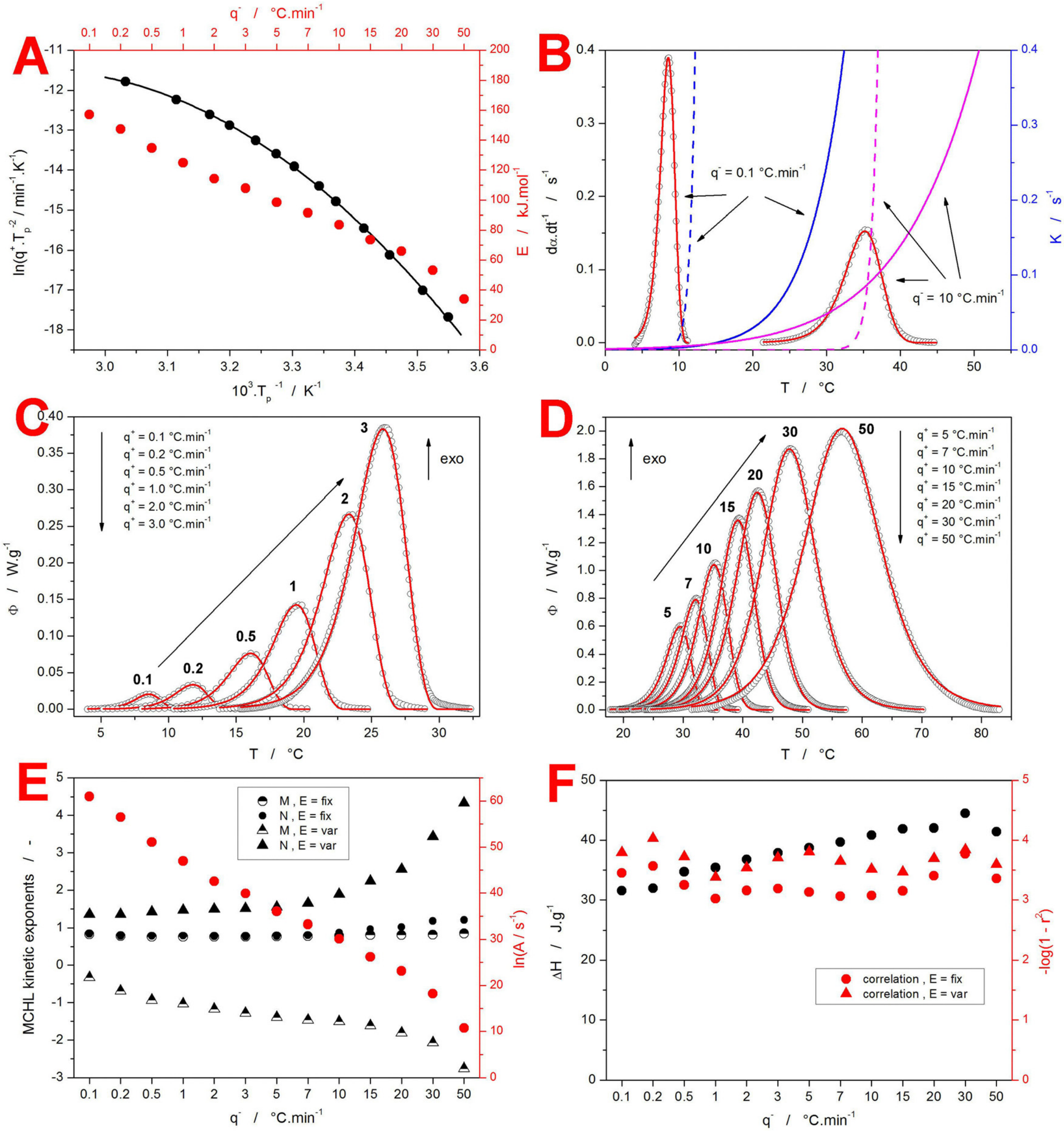

Fig. 9 (A) Kissinger-based determination of E from the glass-heating DSC crystallization experiments (left and bottom axes); evolution of E with applied q^+ (top and right axes). (B) Comparison of the positions of the melt-cooling crystallization peaks (points and red MCHL fitting curves) and the temperature dependence of the corresponding rate constants K (blue and magenta curves). The solid and dashed K–T dependence was calculated with fixed and variable E values, respectively (see text for details). (C) Low-q^+ DSC data (points) fit by the autocatalytic Arrhenian model (red lines). (D) High-q^+ DSC data (points) fit by the autocatalytic Arrhenian model (red lines). (E) and (F) Evolution of different kinetic parameters obtained from the autocatalytic Arrhenian fit of the glass-heating crystallization data from graphs C and D.

dependence is obviously curved; hence, the temperature-dependent E can be obtained by the differentiation according eqn (7) (in a similar way as the temperature dependent K_g in Fig. 8A). Contrary to the unsuccessful implementation of the continuous $K_g(T)$ dependence, calculation accounting for the continuous $E(T)$ dependence gives reasonable courses of the Arrhenian rate constant. Therefore, both alternatives were used, and two series of kinetic optimizations were performed: one with E being fixed at a different constant value for each fitted data-curve (these E values are depicted in Fig. 9A; the approach denoted as "E = fix"), and the other with a single E–T master curve/dependence being directly included in eqn (4) (the approach denoted as "E = var"). Two examples of both courses of the rate constants are shown in Fig. 9B, together with the corresponding crystallization peaks. Clearly, the "E = var" option (the dashed lines) results in a much more abrupt increase of the crystallization rate, which will have to be compensated kinetically (as will be shown below). The full set of the fitted DSC data is shown in Fig. 9C and D.

The results of the two sets of non-linear optimizations based on the combination of eqn (1) and (4) (with either "E = fix" or "E = var") are shown in Fig. 9E and F. Interestingly, practically the same $\ln A$ values were obtained in both optimization series ($\ln A$ was in both series considered a constant for the given data curve, imitating the approach used for hot crystallization in Section 5.1.1), indicating that it is the initial value of the rate constant $K(T)$ that is crucial for the course of the crystallization process. However, there was a striking difference between the two sets of the Šesták–Berggren kinetic exponents M and N, where the "E = fix" option provided nearly constant values of both exponents across the whole range of applied q^+ (again characteristically corresponding[46] to the nucleation-growth kinetics[60,61]), while the "E = var" option leads to the apparently uncommon M and N values, requiring very high N values and negative M values to compensate for the E–A dissonance. Although the accuracy of the kinetic description was slightly higher for the "E = var" option (see the correlation coefficients shown in Fig. 9F), the evident necessity for the multifold mutual compensation of the kinetic parameters does not testify to the correctness of this mathematical solution. Considering the similar findings being obtained for the MCHL model in Section 5.1.1, a conclusion can be drawn that the implementation of the temperature-dependent $K_g(T)$ or $E(T)$ will require compensation by a corresponding $A(T)$ master curve to provide a suitable, physically meaningful description of the crystallization data. This is, however, left for a future endeavor; in the meantime, the currently used approach, also known as the single-curve multivariate kinetic analysis (sc-MKA),[63] based on the present "E = fix" option, will be a viable method for the description of the temperature-dependent kinetic data. Apart from the above-described analysis, it is worth noting that the accurately determined (through utilizing eqn (5)) crystallization enthalpies (see Fig. 9F) are indeed significantly lower during the cold crystallization compared to the hot crystallization (data depicted in Fig. 8F and listed in SI).

5.1.3. **Isothermal annealing.** The evaluation of the isothermal data series (data-curves for every other T_a are depicted in Fig. 2C and D) can be done either in terms of the MCHL model or in terms of the standard solid-state Arrhenian kinetics (combination of eqn (1) and (4)). As the MCHL model is specifically derived for polymeric materials and gives additional information about the nucleation behavior (through the K_g parameter), it was prioritized in the present paper. Similarly to the evaluation of the non-isothermal data, also here, the K_g–T dependence needs to be determined first according to eqn (6). In Fig. 10A, the $t_{0.5}$-based evaluation is shown for both isothermal data series in comparison with the non-isothermal melt-cooling data from Fig. 8A. The non-isothermal dependence characterizing K_g during cooling, and the dependence corresponding to the isotherm following the cooling, relatively well match into a continuous master curve – confirming the equal nature of the two measurements. On the other hand, the dependence corresponding to the isotherm following the heating from the glassy state matches this master curve only at the lowest T_as. This discrepancy is certainly caused by the additional time allowed for the nucleation (possibly enhanced through the pre-formed mesomorphic phase) during the finalization of the cooling step, equilibration at −30 °C, and following heating to T_a. These processes significantly sped up the crystal growth, reducing $t_{0.5}$; the reduction/discrepancy is naturally the larger the higher the T_a (longer additional time in comparison to the melt-cooling type of experiment). This is depicted in the inset of Fig. 10A – the deviations between the two types of experiments occur for T_as $\geq$ 20 °C. Interestingly, both high-T dependencies are of good linearity, providing a constant value of K_g ($\sim 130\,500 \pm 7100$ K^2 for heating from the glass, and $\sim 360\,100 \pm 8500$ K^2 for cooling from the melt). Since the K_g values are, in the case of isothermal data, fully compensated by $\ln A$, the following kinetic calculations were, for the sake of simplicity, performed with these two K_g values also in the low-T region, bearing in mind the possible distortion of $\ln A$.

The identical Levenberg–Marquardt-based non-linear optimization (as used in Section 5.1.1) was used to fit the two isothermal data series by the MCHL model – corresponding rate constants are shown in Fig. 10B, and examples of the quality of the curve-fitting are shown in Fig. 10C and D. Note the almost one order of magnitude increase of $K(T)$ caused by the extra nucleation time provided in the case of cold crystallization experiments – see Fig. 10B. It is worth noting that the largely enhanced nucleation rate can be also a consequence of the mesomorphic phase being possibly formed during the cooling step. However, apart from the large difference in the K_g (and correspondingly also the equalizing $\ln A$) values, the MCHL kinetic exponents M and N as well as the overall crystallization enthalpies are extremely similar for both types of the isothermal experiments – as evidenced in Fig. 10E and F (full sets of kinetic parameters are listed in SI). The interpretation of the M and N values[46] indicates the 3-dimensional interface-controlled crystal growth for both types of isothermal kinetics. The increasing N values observed for high-T annealing

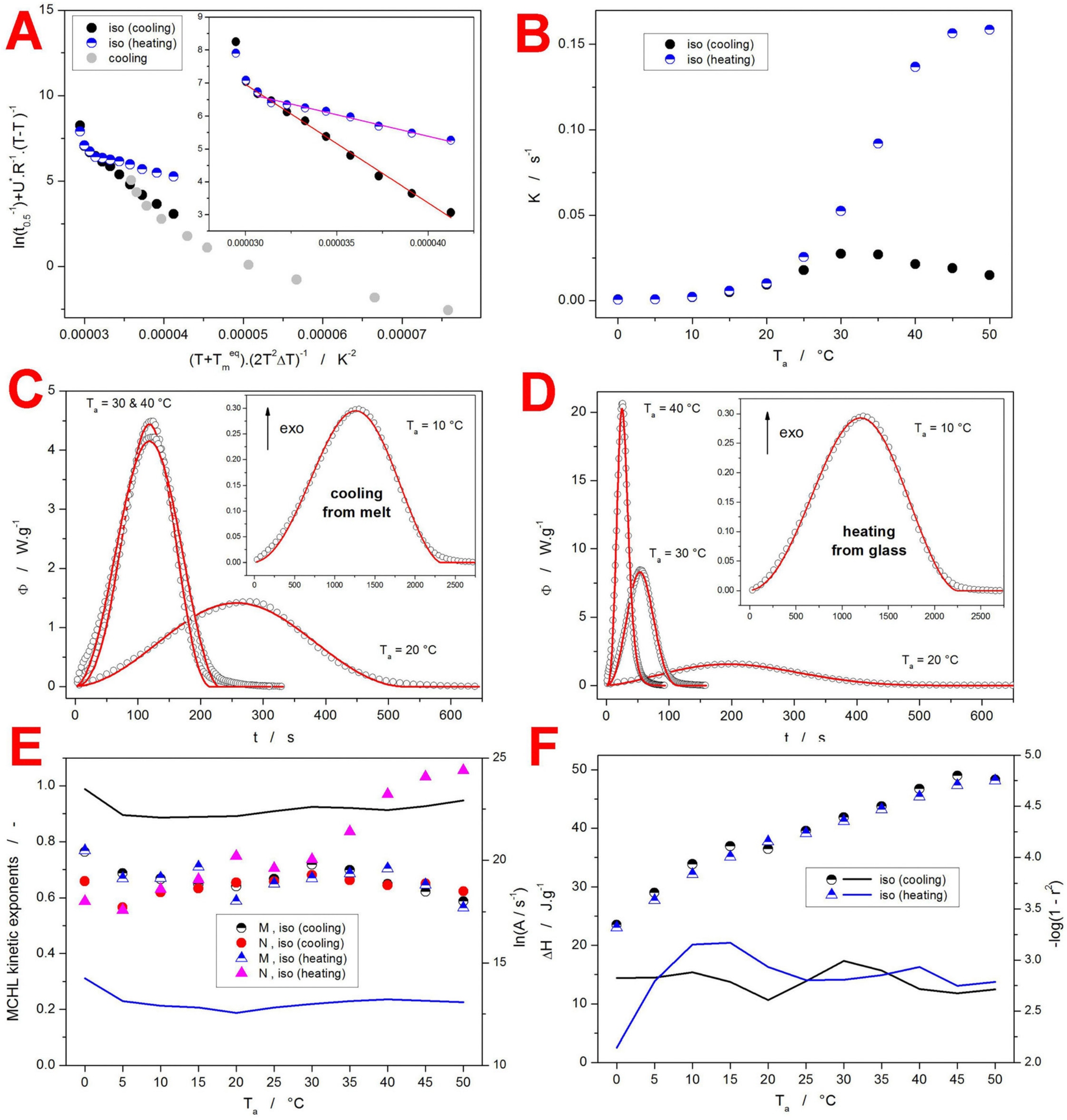

Fig. 10 (A) Determination of K_g from the isothermal DSC crystallization experiments; "iso(cooling)" and "iso(heating)" indicate the cycles, where T_a was reached during the cooling of a melt and during the heating of a glass, respectively. The isothermal data are compared with akin non-isothermal data from Fig. 8A. The inset shows only the zoomed-in isothermal data with their dominant high-T linear parts fit. (B) Temperature dependence of the rate constant K determined in terms of the Hoffman–Lauritzen theory for the two sets of isothermal crystallization data. (C) Selected isothermal crystallization data (points) obtained from the melt-cooling cycles fit by the MCHL model (red lines). (D) Selected isothermal crystallization data (points) obtained from the glass-heating cycles fit by the MCHL model (red lines). (E) and (F) Evolution of different kinetic parameters obtained from the MCHL fit of the isothermal crystallization data. Solid lines are associated with the quantities depicted on the right axes.

following the heating from the glassy state indicate a possible transition towards the diffusion-controlled mechanism (due to the much higher crystallization rate and competition between a large number of active growth sites), rather than the decrease of the morphological dimensionality of the growing crystallites. However the micrographs from Fig. 7 are inconclusive in this regard. Importantly, the isothermal crystallization enthalpy (ΔH–T_a dependence from Fig. 10F) very well corresponds to the akin data from Fig. 9F (considering the shift in the covered temperature ranges), but the isothermal data show a significantly more temperature-distinguished formation of the loosely packed low-T phase with a correspondingly low ΔH.

5.2. Kinetic predictions of PDX crystallization

A comparison between these simulations and real experimental measurements was made to test the relevance and accuracy of the kinetic predictions based on different sets of kinetic parameters determined for the crystallization of PDX. The isothermal measurements performed at 0, 25 and 50 °C (under both setups, *i.e.*, with achieving T_a either from the liquid or from the

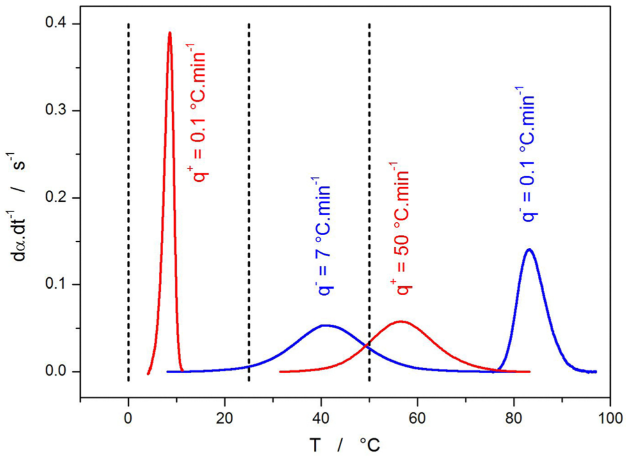

Fig. 11 Depiction of the non-isothermal crystallization data (the parameters of which were used for the kinetic predictions) in comparison with T_as (vertical dashed lines) for which the predictions were made.

glassy state) were used as the experimental verification; the theoretical predictions were then simulated for these T_as using the sets of kinetic parameters obtained from the following curve-fitted data: non-isothermal cooling from the melt at 0.1 and 7 °C min^{-1}, non-isothermal heating from glass at 0.1 and 50 °C min^{-1}, isothermal annealing after cooling from the melt (denoted, *e.g.*, as "$q^- \gg T_a = 0$ °C"), and isothermal annealing after heating from glass (denoted, *e.g.*, as "$q^+ \gg T_a = 0$ °C"). Visualization of the corresponding temperature ranges is shown in Fig. 11. In the case of the non-isothermal data, the two borderline data-curves (the highest and the lowest cooling/heating rates with fully manifesting crystallization peak) were selected for each crystallization pathway; the four crystallization peaks well cover the isothermally investigated range (the T_as of interest are indicated by the dashed lines). The three T_as were selected so that the main difference between the two crystallization pathways (the nucleation-determined crystallization rate; see Fig. 10B) was clearly covered.

The kinetic predictions were aimed to test the following hypotheses: (1) the closer the non-isothermal crystallization peak to the predicted T_a, the better the prediction; (2) the "$q^- \gg T_a$" isothermal predictions are more accurate with the kinetic parameters obtained from the melt-cooling measurements, and the "$q^+ \gg T_a$" predictions are better based on the glass-heating kinetics; (3) the prediction based on the non-isothermal measurement covering a closer T range will be more accurate than the prediction utilizing the isothermal kinetic parameters but from a distanced T_a; (4) the q^-/q^- ranges (0.1–50 °C min^{-1} in the absolute values) explored in the present study are sufficient to provide a reliable basis for all relevant isothermal predictions.

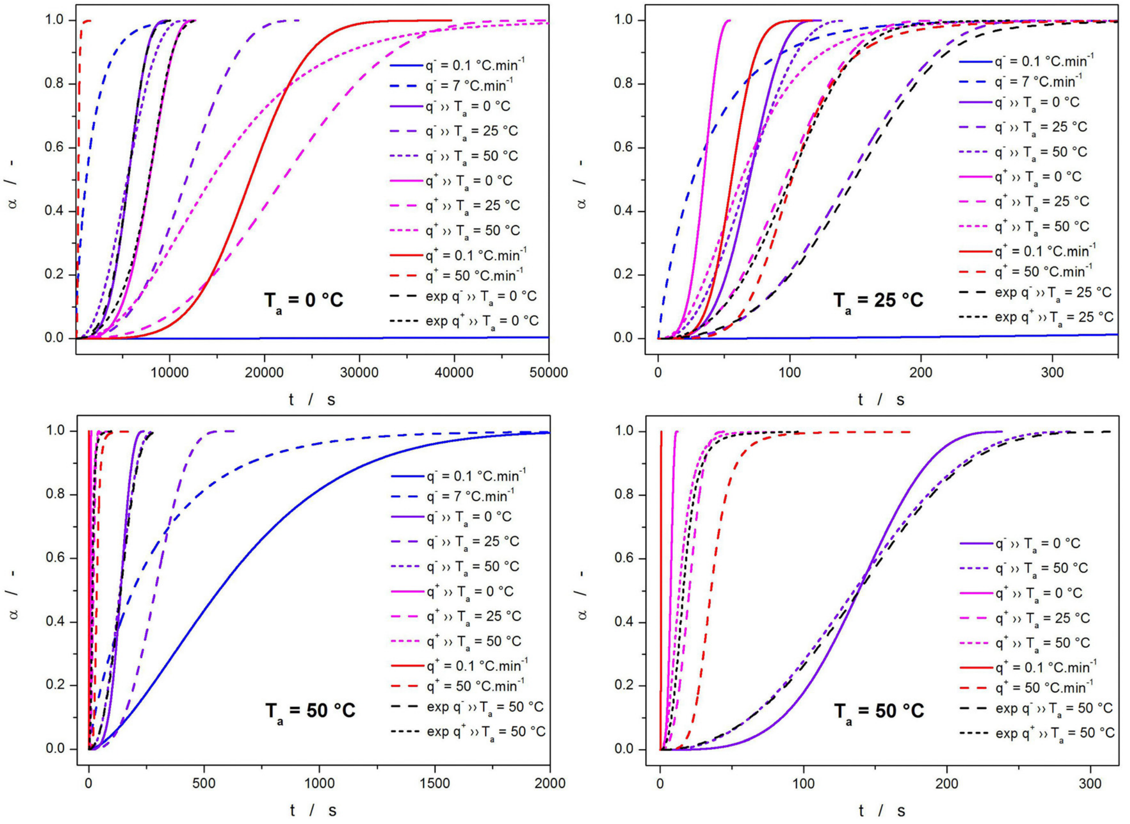

Fig. 12 Kinetic predictions for the three selected T_as; the two graphs for $T_a = 50$ °C show the zoomed and unzoomed versions of the same graph. The denotation "$q^- \gg \ldots$" indicates parameters from isothermal crystallization following the cooling of a melt; similarly, "$q^+ \gg \ldots$" indicates parameters from isothermal crystallization following the heating from the glassy state.

The kinetic predictions for the three selected T_as (0, 25 and 50 °C) are shown in Fig. 12. Starting with the lowest T_a = 0 °C, the theoretically closest non-isothermal measurement is that performed at q^+ = 0.1 °C min^{-1} (during cooling, the crystal growth ceases at linear q^- sufficient to reach 0 °C before the crystallization initiates or is fully completed). However, practically all non-isothermal measurements provide in this case very poor predictions, differing by at least an order of magnitude on the time scale – the closest prediction (but still unusable for any practical purpose) is that calculated from the cooling at 7 °C min^{-1} (*i.e.*, the second closest one in Fig. 11). From the isothermal predictions, the one calculated from "$q^- \gg T_a$ = 50 °C" is quite close to both experimental datasets (the exact "fits" have to be, naturally, ruled out from the comparison) – it is actually closer to the experimental "$q^+ \gg T_a$ = 0 °C" data than is the prediction calculated from the "$q^- \gg T_a$ = 0 °C" kinetic parameters. This is due to the crystallization during cooling obeying the Hoffman–Lauritzen kinetics, where the driving force is comparatively low at very high T (lack of nuclei, low undercooling ΔT) and at very low T (slow diffusion). Therefore, the prediction calculated from the "$q^- \gg T_a$ = 25 °C" parameters significantly deviates from the other two akin calculations. Nonetheless, the match between the two experimental datasets with T_a = 0 °C ("$q^- \gg \ldots$" and "$q^+ \gg \ldots$") is also relatively good, indicating that they can be mutually used to predict each other.

For the isothermal annealing at 25 °C, the difference between the two experimental datasets is already large, as the effect of additional nucleation occurring during the "$q^+ \gg \ldots$" experiment increases. If we again rule out the exact matches (direct fits of the experimental data), then a very good correspondence occurs only between the experimental "$q^+ \gg T_a$ = 25 °C" data and the prediction based on the "q^+ = 50 °C min^{-1}" non-isothermal parameters. A relatively acceptable prediction of the same experimental dataset is also that obtained from the "$q^+ \gg$ 50 °C" parameters; otherwise, relatively poor predictions were obtained, which is quite surprising as T_a = 25 °C lies in the middle of the investigated temperature interval, and should be covered by multiple measured datasets (see Fig. 11). This is most probably due to the inherently T-dependent kinetics as expressed by the curvatures in Fig. 8A and 9A.

In the case of the predictions for isothermal annealing at T_a = 50 °C, a good correspondence is found between the experimental "$q^- \gg T_a$ = 50 °C" data and the prediction based on the "$q^- \gg T_a$ = 0 °C" isothermal parameters (similar case as for the first introduced predictions for T_a = 0 °C). In addition, the experimental "$q^+ \gg T_a$ = 50 °C" data are well predicted by the parameters obtained from the "$q^+ \gg T_a$ = 25 °C" fit. Since the former correlation can be again attributed to the specificity of the Hoffman–Lauritzen kinetics (which accounts for the true non-monotonicity of the K–T dependence), the latter case testifies about the reliability of the polymer crystallization kinetic predictions being mainly associated with the state of nucleation alone: for the "$q^+ \gg \ldots$" series, the material is expected to be already well nucleated and the constant value of K_g (see Fig. 10A) seems to be the deciding factor for the accuracy of the kinetic predictions. Conversely, although the "$q^- \gg \ldots$" series also exhibits linearity (constant K_g) in the given temperature region, the added influence of the ongoing nucleation clearly affects the overall crystallization rate exceedingly for the corresponding T-closest kinetic prediction (from "$q^- \gg$ 25 °C") to be accurate.

6. Conclusions

The crystallization behavior of PDX was investigated under various pathways (during cooling, heating, and isothermal annealing) using DSC measurements complemented by Raman spectroscopy, TGA, and optical microscopy experiments. The continuity of the manifestation of the $\alpha' \rightarrow \alpha$ transition as well as the gradually increasing crystallinity observed *via* Raman measurements (probably due to the lamellae thickening) confirms that no sharp polymorphic transition exists for the PDX crystallization data, which justifies the continuity of the temperature-dependent kinetic modeling. The comparative evaluation of kinetic descriptions revealed that while both the temperature-dependent Hoffman–Lauritzen and Arrhenian approaches can provide good fits to experimental data, their predictive power is strongly dependent on the crystallization pathway and temperature regime. In particular, the melt-crystallization kinetics were governed by the interplay between nucleation and growth processes, leading to non-monotonic dependencies, whereas cold crystallization was more strongly determined by pre-existing nuclei formed during quenching. The overall impact of pre-thermal history is thus demonstrated to be crucial for understanding the difference between the two crystallization pathways.

The kinetic modeling highlighted that reliable predictions require not only careful selection of the appropriate theoretical framework but also consistent treatment of temperature-dependent parameters. Attempts to introduce continuous temperature dependence of the key quantities ($K_g(T)$, $E(T)$) into the models often demanded compensatory adjustments of other parameters, stressing the need for more physically grounded master curve approaches, namely those simultaneously implementing the complementary $A(T)$ dependence. On the other hand, the introduction of the T-dependent exponents of the extended MCHL model was proven to be mandatory for the physically meaningful interpretation of the crystallization kinetics. Furthermore, the present data demonstrated that the accuracy of the kinetic predictions for the isothermal polymer crystallization is dominantly driven by the match of the nucleation states between the training and testing datasets, *i.e.* the data used to determine the kinetic parameters used for the predictions and the actual reality that is being predicted. Accordingly, the thermal proximity (correspondence between the training and testing temperature ranges) is only of secondary importance. These findings emphasize the limitations of using standard non-isothermal measurements for straightforward prediction of isothermal crystallization, especially at temperatures where nucleation becomes rate-determining.

The results suggest that future refinement of universal kinetic models must explicitly integrate the contributions of the temperature-dependent nucleation dynamics to enhance predictive reliability.

Conflicts of interest

The authors declare that they have no known competing financial interests or personal relationships that could have appeared to influence the work reported in this paper.

Data availability

Supplementary information is available. See DOI: https://doi.org/10.1039/d5cp04749h.

The data are available in the FigShare database under DOI: https://doi.org/10.6084/m9.figshare.30138169.

Acknowledgements

This work has been supported by the Ministry of Education, Youth and Sports of the Czech Republic (project LM2023037). The author is grateful to Assoc. Prof. Jana Machotová (University of Pardubice, Czech Republic) for her cordial and greatly inspiring discussions.

References

1 O. Attallah, A. Janssens, M. Azeem and M. Fournet, Fast, high monomer yield from post-consumer polyethylene terephthalate via combined microwave and deep eutectic solvent hydrolytic depolymerization, *ACS Sustainable Chem. Eng.*, 2021, **9**, 17174–17185.
2 Y. Ko, J. Hinestroza and T. Uyar, Structural investigation on electrospun nanofibers from postconsumer polyester textiles and pet bottles, *ACS Appl. Polym. Mater.*, 2023, **5**, 7298–7307.
3 X. Zhao, T. Liao, Y. Lu, Z. Jiang and Y. Men, Formation and distribution of the mesophase in ultrasonic micro-injection-molded isotactic polypropylene, *Macromolecules*, 2021, **54**, 5167–5177.
4 N. Tan, L. Lin, T. Deng and Y. Dong, Evaluating the residual stress and its effect on the quasi-static stress in polyethylene pipes, *Polymers*, 2022, **14**, 1458.
5 S. Lee, S. Yoon, J. Baek and I. Jeon, Preparation of hexene-functionalized graphitic nanoplatelets for effective interaction with nylon 6, *J. Reinf. Plast. Compos.*, 2022, **42**, 819–827.
6 T. Lee, H. Yu, M. Forrester, T. Wang, L. Shen and H. Liu, *et al.*, Next-generation high-performance bio-based naphthalate polymers derived from malic acid for sustainable food packaging, *ACS Sustainable Chem. Eng.*, 2022, **10**, 2624–2633.
7 R. Abedi, B. Maher, L. Amirkhani, M. Rezaei and S. Jamshidi, The relationship between chemical microstructure, crystallinity, mechanical properties, and CO2/N2 gases permselectivity of thermoplastic polyurethane membranes, *Colloid Polym. Sci.*, 2024, **302**, 1081–1095.
8 R. Xu, L. Yin, J. Chen, J. Xie, Z. Yin and C. Lei, The effect of melt drawing ratio on the crystal structural change and performance of polyketone extrusion cast film, *J. Polym. Sci.*, 2022, **60**, 2465–2475.
9 M. Xue, K. Lv, S. Gao, X. Lu, Y. Liu and S. Yan, Synergistic effect of thermoplastic phenolic resin and multiwalled carbon nanotubes on the crystallization of polyoxymethylene, *J. Polym. Sci.*, 2020, **58**, 997–1010.
10 H. Neve, S. Thorat and S. Radhakrishnan, Melt processing behaviour and structure development in recycled pp blends with recycled pet, *Prog. Rubber, Plast. Recycl. Technol.*, 2022, **39**, 141–155.
11 J. Amaya, Determination of time and concentration conditions affecting polylactic acid (PLA) production, *Polymers*, 2025, **17**, 2009.
12 F. Aliberti, M. Oliviero, R. Longo, L. Guadagno and A. Sorrentino, Effect of crystallinity on the printability of poly(ethylene terephthalate)/poly(butylene terephthalate) blends, *Polymers*, 2025, **17**, 156.
13 P. Kothavade, P. Yadav, A. Gopal, H. Pol, A. Kafi and S. Bateman, *et al.*, Enhancing the crystallization kinetics and mechanical properties of poly(lactic acid) blends for 3D printing application, *ACS Appl. Polym. Mater.*, 2024, **6**, 5754–5762.
14 F. Santos, B. Hernandez, R. Santos, M. Machado, M. Souza and E. Sousa, *et al.*, Bioabsorbable polymeric stent for the treatment of coarctation of the aorta (coa) in children: a methodology to evaluate the design and mechanical properties of PLA polymer, *Materials*, 2023, **16**, 4403.
15 T. Czelusniak and F. Amorim, Influence of energy density on polyamide 12 processed by sls: from physical and mechanical properties to microstructural and crystallization evolution, *Rapid Prototyping J.*, 2021, **27**, 1189–1205.
16 C. Zhang, W. Wu, H. Hu, Z. Rui, J. Ye and H. Shên, Effect of multidimensional filler hybridization on the mechanical properties of thermoplastic polyurethane composites prepared by selective laser sintering, *J. Appl. Polym. Sci.*, 2023, **140**, e54041.
17 W. Han, L. Kong and M. Xu, Advances in selective laser sintering of polymers, *Int. J. Extreme Manuf.*, 2022, **4**, 042002.
18 A. Vollrath, C. Kretzer, B. Beringer-Siemers, B. Shkodra, J. Czaplewska and D. Bandelli, *et al.*, Effect of crystallinity on the properties of polycaprolactone nanoparticles containing the dual flap/mpegs-1 inhibitor brp-187, *Polymers*, 2021, **13**, 2557.
19 Z. Azhari, P. Smith, S. McMahon, W. Wang and R. Cameron, Modulating drug release from short poly(ethylene glycol) block initiated poly(l-lactide) di-block copolymers, *Pharm. Res.*, 2022, **40**, 1697–1707.
20 J. Loskot, D. Jezbera, Z. Zmrhalová, M. Nalezinková, D. Alferi and K. Lelkes, *et al.*, A complex in vitro degradation study on polydioxanone biliary stents during a clinically relevant period with the focus on Raman spectroscopy validation, *Polymers*, 2022, **14**, 938.

21 F. Ronkay, D. Gere, E. Slezák, E. Szabó, G. Marosi and K. Bocz, Recycled pet packaging materials of improved toughness—importance of devitrification of the rigid amorphous fraction, *Macromol. Mater. Eng.*, 2024, **310**, 2400219.

22 J. Sun, W. Zhang, F. Li, Q. Zhuo, C. Qin and J. Wang, *et al.*, Effect of heat treatment with alternating tension on microstructure and elastic recovery of poly(trimethylene terephthalate) fibers, *Polym. Adv. Technol.*, 2022, **33**, 2425–2433.

23 S. Kanomi, H. Marubayashi, T. Miyata and H. Jinnai, Reassessing chain tilt in the lamellar crystals of polyethylene, *Nat. Commun.*, 2023, **14**, 5531; J. D. Hoffman, G. T. Davis and J. I. Lauritzen, Jr., in *Treatise on Solid State Chemistry*, ed. N. B. Hannay, Plenum, New York, 1976, vol. 3, p. 497.

24 J. Xia, L. Ni, C. Zeng, B. Wang, R. Zhang and C. Sun, *et al.*, Temperature-Dependent Triple Crystal Polymorphism of Poly(hexamethylene terephthalate): Long-Range Ordered Mesophase Formation and Crystal Structure–Property Relationships, *Macromolecules*, 2024, **57**, 7369–7380; J. D. Hoffman and J. J. Weeks, Melting process and the equilibriummelting temperature of polychlorotrifluoroethylene, *J. Res. Natl. Bur. Stand., Sect. A*, 1962, **66**, 13–28.

25 J. Sheng, W. Chen, K. Cui and L. Li, Polymer crystallization under external flow, *Rep. Prog. Phys.*, 2022, **85**, 036601; M. Burger and V. Capasso, Mathematical modelling and simulation of non-isothermal crystallization of polymers, *Math. Models Methods Appl. Sci.*, 2001, **11**, 1029–1053.

26 F. Peng, R. Cao, H. Sun, Z. Liu, Y. Zhang and T. Xu, *et al.*, Role of Entanglement in Polymer Crystal Growth and Melting: Molecular Dynamics Simulations, *Macromolecules*, 2024, **57**, 10487–10498; M. Arshad, A novel kinetic approach to crystallization mechanisms in polymers, *Polym. Eng. Sci.*, 2021, **61**, 1502–1517.

27 I. Tzourtzouklis, P. Kardasis, G. Papageorgiou and G. Floudas, Phase Diagram, Glassy Dynamics and Crystallization Kinetics of the Biobased Polyester Poly(ethylene 2,5-furanoate) (PEF), *Macromolecules*, 2024, **57**, 11395–11406; R. Svoboda and J. Machotová, Polymer Crystallization: Universal Macroscopic Description via the Autocatalytic Hoffman-Lauritzen Approach, *ACS Omega*, 2025, **10**, 16602–16619.

28 K. Hall, S. Percec, W. Shinoda and M. Klein, Property Decoupling across the Embryonic Nucleus–Melt Interface during Polymer Crystal Nucleation, *J. Phys. Chem. B*, 2020, **124**, 4793–4804; R. Svoboda and J. Machotová, Correction to: Polymer Crystallization: Universal Macroscopic Description via the Autocatalytic Hoffman-Lauritzen Approach, *ACS Omega*, 2025, **10**, 56870.

29 L. Ni, C. Sun, S. Xu, W. Xiang, Y. Pan and B. Wang, *et al.*, Thermally Induced Phase Transition of Polybutene-1 from Form I′ to Form II through Melt Recrystallization: Crucial Role of Chain Entanglement, *Macromolecules*, 2023, **56**, 1973–1982; J. Šesták, *Science of Heat and Thermophysical Studies: A Generalized Approach to Thermal Analysis*, Elsevier, Amsterdam, 2005.

30 Y. Liao and Q. Lan, Understanding the Impact of Chain Mobility on Conformational Evolution and Kinetics of Mesophase Formation in Poly(L-lactide) under Low-Pressure CO2″, *Polymers*, 2024, **16**, 1378; J. Farjas and P. Roura, Modification of the Kolmogorov–Johnson–Mehl–Avrami rate equation for non-isothermal experiments and its analytical solution, *Acta Mater.*, 2006, **54**, 5573–5579.

31 R. Cao, F. Peng, C. Nie, Y. Zhang, H. Sun and Z. Liu, *et al.*, Primary Nucleation of Polymer Crystal via Particles Fluctuation with Non-Markovian Effect, *Macromolecules*, 2024, **57**, 5979–5990; K. Nakamura, T. Watanabe, K. Katayama and T. Amano, Some aspects of non-isothermal crystallization of polymers—Part I: Relationship between crystallization temperature, crystallinity and cooling conditions, *J. Appl. Polym. Sci.*, 1972, **16**, 1077–1091.

32 L. Zou and W. Zhang, Molecular Dynamics Simulations of the Effects of Entanglement on Polymer Crystal Nucleation, *Macromolecules*, 2022, **55**, 4899–4906; R. Svoboda, J. Machotová, M. Krbal, D. Jezbera, M. Nalezinková, J. Loskot and A. Bezrouk, Complex thermokinetic characterization of polydioxanone for medical applications: Conditions for material processing, *Polymer*, 2023, **277**, 125978.

33 S. Nagarajan, K. Huang, W. Chuang, J. Lin and E. Woo, Thermo-Sensitive Poly(p-dioxanone) Banded Spherulites with Controllable Patterns for Iridescence, *J. Phys. Chem. C*, 2023, **127**, 2628–2638.

34 M. Hakim, N. Nahar, M. Saha, S. Islam, H. Reza and S. Sharker, Local drug delivery from surgical thread for area-specific anesthesia, *Biomed. Phys. Eng. Express*, 2020, **6**, 015028.

35 H. Zheng, H. Peng, P. Wang, H. Li, L. Li, Y. Du and G. Lv, In vitro and in vivo evaluation of degradability and biocompatibility of poly(p-dioxanone) hemostatic clips for laparoscopic surgery, *J. Appl. Polym. Sci.*, 2021, **138**, 50772.

36 F. Zhao, H. Xu, W. Xue, Y. Li, J. Sun and F. Wang, *et al.*, Iodinated poly(p-dioxanone) as a facile platform for x-ray imaging of resorbable implantable medical devices, *J. Biomater. Appl.*, 2020, **35**, 39–48.

37 J. Šesták, Šesták–Berggren equation: now questioned but formerly celebrated—what is right, *J. Therm. Anal. Calorim.*, 2017, **127**, 1117–1123.

38 F. Liu and G. Yang, Effects of anisotropic growth on the deviations from Johnson–Mehl–Avrami kinetics, *Acta Mater.*, 2007, **55**, 1629–1639.

39 T. Huang and C. Zhou, Surface Diffusion-Controlled Jonhson–Mehl–Avrami–Kolmogorov Model for Hydrogenation of Mg-based Alloys, *J. Phys. Chem. C*, 2023, **127**, 13900–13910.

40 M. Castro, F. Domínguez-Adame, A. Sánchez and T. Rodríguez, Model for crystallization kinetics: Deviations from Kolmogorov–Johnson–Mehl–Avrami kinetics, *Appl. Phys. Lett.*, 1999, 2205–2207.

41 A. Kolb-Telieps and T. Shu-Song, Investigations to explain the restricted validity of the Avrami-Johnson-Mehl theory for the crystallization of Zr70Ni30, *J. Non-Cryst. Solids*, 1988, **107**, 122–127.

42 K. Shirzad and C. Viney, Revisiting time-dependent growth and nucleation rates in the Johnson-Mehl-Avrami-Kolmogorov equation, *R. Soc. Open Sci.*, 2025, **12**, 241696.

43 M. Fanfoni and M. Tomellini, Beyond the Kolmogorov Johnson Mehl Avrami kinetics: inclusion of the spatial correlation, *Eur. Phys. J. B*, 2003, **34**, 331–341.

44 J. Šesták, *Thermophysical Properties of Solids, Their Measurements and Theoretical Analysis*, Elsevier, Amsterdam, 1984.

45 R. Svoboda, Johnson-Mehl-Avrami kinetics as a universal description of crystallization in glasses?, *J. Eur. Ceram. Soc.*, 2024, **44**, 4064–4082.

46 R. Svoboda, On the path to a universal model for crystallization kinetics: Interpretation of the Šesták-Berggren equation in terms of the nucleation-growth concept, *J. Eur. Ceram. Soc.*, 2026, **46**, 117716.

47 X. Liu, S. Feng, X. Wang, J. Qi, D. Lei, Y. Li and W. Bai, Tuning the mechanical properties and degradation properties of polydioxanone isothermal annealing, *Turk. J. Chem.*, 2020, **44**, 1430–1444.

48 K. Ishikiriyama, M. Pyda, G. Zhang, T. Forschner, J. Grebowicz and B. Wunderlich, Heat capacity of poly-p-dioxanone, *J. Macromol. Sci., Part B:Phys.*, 1998, **37**, 27–44.

49 M. Lorenzo and M. Righetti, Crystallization-induced formation of rigid amorphous fraction, *Polym. Cryst.*, 2018, **1**, e10023.

50 X. Monnier, D. Cavallo, M. Righetti, M. Lorenzo, S. Marina and J. Martín, *et al.*, Physical aging and glass transition of the rigid amorphous fraction in poly(l-lactic acid), *Macromolecules*, 2020, **53**, 8741–8750.

51 J. Lee, J. Mangalara and D. Simmons, Correspondence between the rigid amorphous fraction and nanoconfinement effects on glass formation, *J. Polym. Sci., Part B: Polym. Phys.*, 2017, **55**, 907–918.

52 R. Svoboda and J. Machotová, How Depolymerization-Based Plasticization Affects the Process of Cold Crystallization in Poly(P-Dioxanone), *Macromol. Rapid Commun.*, 2024, **45**, 2400369.

53 J. Martín, N. Stingelin and D. Cangialosi, Direct Calorimetric Observation of the Rigid Amorphous Fraction in a Semiconducting Polymer, *J. Phys. Chem. Lett.*, 2018, **9**, 990–995.

54 J. Loskot, D. Jezbera, A. Bezrouk, R. Doležal, R. Andrýs, V. Francová, D. Miškář and A. Myslivcová Fučíková, Raman Spectroscopy as a Novel Method for the Characterization of Polydioxanone Medical Stents Biodegradation, *Materials*, 2021, **14**, 5462.

55 M. Jaidann and J. Brisson, Conformation Study of poly(p-dioxanone) fibers by polarized Raman spectroscopy, X-ray diffraction, and conformation analysis, *J. Polym. Sci., Part B:Polym. Phys.*, 2008, **46**, 406–417.

56 B. Schrader, *Infrared and Raman Spectroscopy—Methods and Applications*, VCH, Weinheim, Germany, 1995.

57 J. D. Hoffman and J. I. Lauritzen, Jr., Crystallization of bulk polymers with chain folding: theory of growth of lamellar spherulites, *J. Res. Natl. Bur. Stand., Sect. A*, 1961, **65A**, 297–336.

58 K. Levenberg, A method for the solution of certain nonlinear problems in least squares, *Q. Appl. Math.*, 1944, **2**, 164–168.

59 D. W. Marquardt, An algorithm for least-squares estimation of nonlinear parameters, *J. Soc. Ind. Appl. Math.*, 1963, **11**, 431–441.

60 W. A. Johnson and K. F. Mehl, Reaction kinetics in processes of nucleation and growth, *Trans. Am. Inst. Min., Metall. Eng.*, 1939, **135**, 416–442.

61 M. Avrami, Granulation, phase change, and microstructure – kinetics of phase change III, *J. Chem. Phys.*, 1941, **7**, 177–184.

62 H. E. Kissinger, Reaction kinetics in differential thermal analysis, *Anal. Chem.*, 1957, **29**, 1702–1706.

63 R. Svoboda, J. Chovanec, S. Slang, L. Beneš and P. Konrád, Single-curve multivariate kinetic analysis: Application to the crystallization of commercial Fe-Si-Cr-B amorphous alloys, *J. Alloys Compd.*, 2022, **889**, 161672.